



XFEM-based cohesive zone approach for modeling near-wellbore hydraulic fracture complexity

Yongcun Feng¹ · K. E. Gray¹

Received: 12 July 2017 / Accepted: 5 March 2018 / Published online: 26 March 2018
© Springer-Verlag GmbH Germany, part of Springer Nature 2018

Abstract

Near-wellbore fracture tortuosity has important impacts on the productivity of fractured oil and gas wells and the injectivity of CO₂ or solids disposal injectors. Previous models for simulating near-wellbore fracture tortuosity usually assume fracture growth in linear-elastic media, without considering the effects of porous features of the rock. In this paper, a 2D fully coupled model is developed to simulate near-wellbore fracturing using the XFEM-based cohesive segment method. The model takes into account a variety of crucial physical aspects, including fracture extension and turning, fluid flow in the fracture, fluid leak-off through wellbore wall and fracture surfaces, pore fluid flow, and rock deformation. The proposed model was verified against two sets of published experimental results. Numerical examples were carried out to investigate the effects of various parameters on near-wellbore fracture trajectory, injection pressure, and fracture width. Results show that near-wellbore fracture behaviors are not only dependent on rock elastic properties and field stresses, but also greatly influenced by porous properties of the rock, such as permeability and leak-off coefficient. Some field implications were provided based on the simulation results. By overcoming some limitations of the previous models, the proposed model predicts more realistic fracture evolution in the near-wellbore region and provides an attractive tool for design and evaluation of many field operations, for which near-wellbore fracture behaviors play an important role on their successes.

Keywords Cohesive zone model · Fracture complexity · Near-wellbore fracture · Poroelastic effect · XFEM

1 Introduction

It is generally believed that a hydraulic fracture emanating from a wellbore may have a more tortuous pathway in the near-wellbore region than that in the far-field region [45]. This is particularly true if the fracture initiates from a preexisting natural flaw or perforation on the wellbore wall which is not aligned with the preferred fracture direction (direction perpendicular to the minimum horizontal stress for vertical wellbores). In such cases, the fracture can have a complex trajectory in the wellbore vicinity before it eventually reorients to the preferred direction.

Near-wellbore fracture tortuosity has important impacts on a variety of fracturing-related operations in the oil and gas industry. For example, in hydraulic fracturing

treatments, tortuosity-induced fracture width restriction, proppant placement difficulty, injection pressure increase, and unplanned screenout could be fatal to the success of the treatments [14, 45]. Near-wellbore fracture complexity also leads to difficulties in interpretations of field injectivity tests, e.g., leak-off tests, extended leak-off tests, mini-frac tests, pump-in/flow-back tests, and diagnostic fracture injection tests. In these tests, pressure versus time curves are usually interpreted to obtain the desired formation information. For example, the breakdown pressure in an extended leak-off test has commonly been used in the drilling community as a measurement of the minimum field principal stress. However, a tortuous fracture initiating from a natural flaw on the wellbore wall with different orientations with respect to the preferred fracture direction could allow a wide range of breakdown pressures, resulting in considerable ambiguity in test interpretation [27]. For another example, in pump-in/flow-back tests in low permeability formations, fracture closure pressure is measured by implementing a flow-back phase. However, fracture

✉ Yongcun Feng
yongcun.f@gmail.com

¹ Petroleum and Geosystems Engineering Department, The University of Texas at Austin, Austin, USA

tortuosity and width restriction can cause early closure of the fracture in the near-wellbore region during flow-back, while the main body of the fracture remains open, resulting in incorrect (overestimated) fracture closure pressure. Knowledge of near-wellbore fracture behaviors is also important for understanding lost circulation mechanisms and design of wellbore strengthening treatment, an approach to prevent lost circulation during drilling [15, 18]. One of the common practices of wellbore strengthening is to bridge the lost circulation fractures with lost circulation materials (LCMs) to increase fracture propagation resistance and hoop stress around the wellbore. Successful bridging of the fractures requires the use of appropriate LCM particle size distribution (PSD). So information on near-wellbore fracture dimensions, width distribution especially, is important for the PSD design of LCMs. In addition, fracture tortuosity may also affect fracture bridging. According to lessons learned from near-wellbore fracture screenout due to proppant bridging in hydraulic fracturing treatments, a more tortuous fracture should be relatively easier to be bridged in wellbore strengthening treatments thanks to larger fracture curvature and restricted fracture width.

Therefore, the ability to predict near-wellbore behaviors is important for these fracturing-related issues in the petroleum industry. Different from planar fractures that may be characterized by analytical models, e.g., the PKN and KGD fracture models, curving fractures in the near-wellbore region are very difficult, if not impossible, to describe using an analytical approach. For this reason, significant efforts have been devoted to developing numerical models to simulate near-wellbore fractures by means of different numerical approaches in the past few years. Cherny et al. [12] proposed a 2D finite-difference model for this problem. However, the curvilinear fracture path in their model must be prescribed, which significantly limits the applicability of the model. Zhang et al. [51, 52] used a 2D displacement discontinuity model to simulate fracture growth from a wellbore by coupling fluid flow in the fracture and rock deformation. The model was used to investigate the roles of fluid viscosity and injection rate on the tortuosity of near-wellbore fractures. However, their model assumes the formation is linearly elastic material, without considering poroelastic effect, pore fluid flow, and fluid leak-off across the fracture surfaces. As will be illustrated in this paper, porous properties of the formation, e.g., permeability and leak-off coefficient, can have great impact on fracture trajectory, fracture width, and injection pressure. Abdollahipour et al. [2] simulated the propagation of multiple completing hydraulic fractures from a wellbore using a 2D displacement discontinuity model as well. The model also assumes linearly elastic formation and, furthermore, ignores the viscous pressure drop in the fractures. Gordeliy

et al. [20] used a 2D XFEM (extended finite element method) model to investigate near-wellbore fracture reorientation. The model couples fluid flow in the fracture and rock deformation and captures arbitrary fracture paths without explicit remeshing. Nevertheless, their model for rock deformation is also based on linear elasticity.

A number of numerical methods have been used to simulate hydraulic fracture propagation in petroleum engineering community, such as finite element method (FEM) [16, 17, 20, 23, 53, 57], boundary element method (BEM) [25, 46, 47, 49], and discrete element method (DEM) [3, 9, 55, 56]. BEM has the advantage of efficient calculation because only fracture faces are discretized; however, its application is usually restricted to linear-elastic materials [24, 28]. DEM can handle complex fracture patterns and reveal detailed physics regarding the interactions between rock particles and fluids during hydraulic fracturing; but it is more expensive in computation and time-consuming in calibration of material constants compared with FEM and BEM. Methods within FEM framework mainly include adaptive remeshing method, cohesive interface element method, and extended finite element methods. Adaptive remeshing method involves a non-trivial remeshing process while modeling fracture propagation. Cohesive interface element method requires assigning of interface elements at the edges of bulk elements, which has been extensively used to model hydraulic fracture growth along a pre-known and pre-defined path in petroleum engineering, although it can be used to model arbitrary fracture propagation if interface elements are inserted at each element edge [28]. In this paper, XFEM is applied. XFEM can handle complex fracture patterns without the need of remeshing and additional interface elements, providing an attractive method for modeling fracture tortuosity in the near-wellbore region. A cohesive zone model (similar to that used in the cohesive interface element method by Nguyen et al. [28]) is used in conjunction with XFEM to model fracture evolution because it eliminates the crack tip singularity of linear-elastic fracture mechanics (LEFM). In addition, a cohesive zone model can directly predict fracture propagation by satisfying global equilibrium, while LEFM may need iterations to accurately predict how far a fracture can propagate at each time step [24]. For simplicity, we do not consider micro-branch instability and fluid lag in the cohesive zone model. Interested readers are referred to [31] for details on micro-branch instability and to [19] for fluid lag.

It is also worth mentioning some other interesting numerical methods for modeling complex fracture patterns. For example, cracking particle method (CPM) [29, 30, 32] has been developed to model arbitrary evolving fractures without the need of enrichment as XFEM. In CPM, the

fracture is treated as a collection of cracked particles with a discontinuity at each cracked particle. The fracture criterion is checked independently at each particle and thus the method is able to capture complex fracture branching and intersections. Another method for modeling complex fractures is peridynamics (PD) [34, 35, 37]. In PD, fractures occur naturally during simulation and no representation of fracture topology is needed, making it easy to simulate complex fracture patterns. The traditional PD method was first proposed by Silling [37], which requires the horizon sizes to be constant to avoid spurious wave reflections and ghost forces between particles. Ren et al. [34] improved the method and presented the so-called Dual-horizon peridynamics (DH-PD) method based on the concept of horizon and dual horizon to remove the issue of varying horizons and ghost force. However, the application of these novel methods in modeling hydraulic fracturing is still rare. For FEM-based computational fracture problems, there are great improvements in the meshing techniques recently. For example, an edge-based mesh refinement method is proposed in [4, 5]. Interested readers are referred to [4–7] for recent developments in efficient remeshing techniques.

For hydraulic fracture propagation from a 2D plane-strain wellbore in a linearly elastic media (Fig. 1) without considering poroelastic effects, the severity of fracture curving in the near-wellbore region can be characterized by a dimensionless parameter β when the fracture growth is dominated by fracture toughness [27] and by a dimensionless parameter χ_F when the fracture growth is viscosity dominated [22]. β and χ_F can be expressed as:

$$\beta = \frac{(S_H - S_h)\sqrt{R}}{K_{IC}} \quad (1)$$

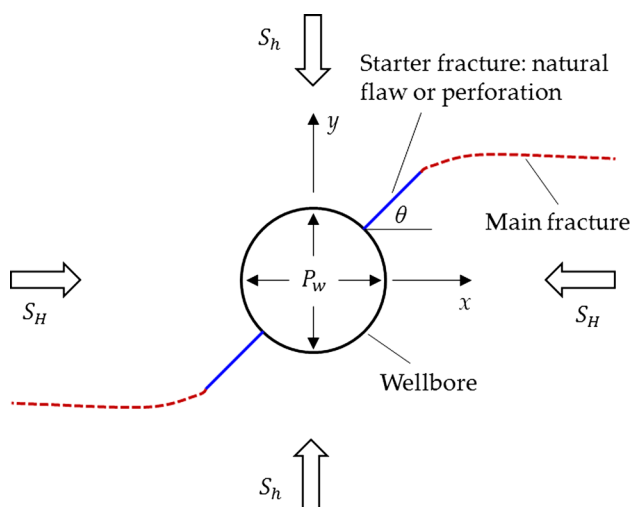


Fig. 1 Hydraulic fractures emanating from a circular wellbore (modified after [51])

$$\chi_F = \frac{(S_H - S_h)\sqrt{R}}{(\mu'QE'^3)^{1/4}} \quad (2)$$

where S_H and S_h are the maximum and minimum horizontal stresses, respectively; K_{IC} is rock fracture toughness; R is wellbore radius; $\mu' = 12\mu$ is scaled fluid viscosity; μ is dynamic fluid viscosity; $E' = \frac{E}{1-\nu^2}$ is plane-strain modulus; E and ν are Young's modulus and Poisson's ratio of the rock, respectively; and Q is injection rate into the fracture. In general, the toughness- and viscosity-dominated fracture growth conditions can be identified by a dimensionless toughness κ (Eq. 3): fracture growth is toughness-dominated if $\kappa > 4$ and viscosity-dominated if $\kappa < 1$ [13].

$$\kappa = \frac{K'}{(\mu'QE'^3)^{1/4}} \quad (3)$$

where $K' = 4K_{IC}\sqrt{\frac{2}{\pi}}$ is a scaled fracture toughness; the other parameters are the same as defined above.

Regardless of the fracture growth regime, Eqs. 1 and 2 indicate that, for a certain wellbore, fracture curving in the near-wellbore region is only dependent on far-field stresses, rock mechanical properties, and injection parameters. However, these equations only apply to fracture growth in linearly elastic, impermeable media. As has been mentioned above and will be shown later in this paper, in poroelastic formations, the porous features of rock will also significantly influence the near-wellbore fracturing, and thus the dimensionless parameters of Eqs. 1 and 2 are not sufficient in characterizing the near-wellbore fracture curving.

This paper develops a 2D fully coupled model which is able to take into account a variety of crucial physical aspects during hydraulic fracture growth in the near-wellbore region, including fracture extension and turning, fluid flow in the fracture, fluid leak-off through wellbore wall and fracture surfaces, pore fluid flow, and rock deformation. A cohesive segment model is used for capturing fracture extension and the associated fracture fluid flow and leak-off. Rock deformation and pore fluid flow are modeled based on poroelasticity theory and Darcy's law. The different components are incorporated into a XFEM framework using the finite element code Abaqus. By doing this, the XFEM model can simulate arbitrary fracture growth paths while considering fluid dynamics in the fracture and poroelastic behavior of the rock. In the following, the basic equations used in the proposed model are first presented. Then, the model is verified against published experimental results in the literature. Next, simulations of near-wellbore fractures under various conditions are performed and effects of some key factors on the fracture behaviors are investigated based on the simulation results. This paper concludes

with a discussion of the model capability and implications of the simulation results on relevant field operations.

2 Methodology

To model hydraulic fracture propagation in porous formation, three components should be coupled and modeled simultaneously: (1) deformation of porous formation (including fracture opening), (2) fluid flow in porous formation, and (3) fluid flow in the fracture. For simplicity, we restrict the current model to 2D, isotropic, and homogenous formation fully saturated with a single-phase fluid. The model does not account for fluid lag (i.e., the fluid front in the fracture is identical to the fracture front). We also do not consider crack branching which can be important in hydraulic fracturing simulations, especially for modeling intersections between hydraulic fractures and natural fractures, topics beyond the scope of this paper. In this section, we provide the governing equations, weak forms, FEM discretization, and some implementation aspects of the coupled near-wellbore fracture problem.

2.1 Governing equations

2.1.1 Deformation of porous formation

The formation is assumed to be an isotropic, homogeneous, and poroelastic medium, fully saturated with a single-phase fluid. The equilibrium equation without body force is stated in the strong form as

$$\nabla \cdot \boldsymbol{\sigma} = 0 \quad (4)$$

where $\boldsymbol{\sigma}$ is the total stress tensor. According to poroelasticity theory [41], the total stress is related to effective stress and pore pressure as

$$\boldsymbol{\sigma}' = \boldsymbol{\sigma} + \alpha p \mathbf{I} \quad (5)$$

where $\boldsymbol{\sigma}'$ is the effective stress tensor, p is the pore pressure, α is the Biot's coefficient, and \mathbf{I} is the unit tensor.

2.1.2 Fluid flow in porous formation

The continuity equation for pore fluid flow in the porous formation can be expressed as

$$\frac{1}{M} \dot{p} + \alpha \nabla \cdot \dot{\mathbf{u}} + \nabla \cdot \mathbf{v}_d = 0 \quad (6)$$

where M is the Biot's modulus, \mathbf{u} is the displacement of the solid phase, \mathbf{v}_d is the fluid flow velocity of the pore fluid. The fluid flow is assumed to obey Darcy's law as

$$\mathbf{v}_d = -\frac{\mathbf{k}}{\mu} \nabla p \quad (7)$$

where μ is the viscosity of pore fluid, \mathbf{k} is the permeability tensor. In this study, rock permeability is assumed to be isotropic.

2.1.3 Fluid flow in the fracture

Upon the opening of a hydraulic fracture, fluid will flow into the fracture with two components: tangential flow along the fracture and normal flow (fluid leak-off) from the fracture surfaces into the formation. Assuming incompressible fluid, the continuity equation of fracture fluid flow is expressed as

$$\dot{w} + \frac{\partial q}{\partial s} + q_t + q_b = 0 \quad (8)$$

where w is the fracture width (aperture), q is the tangential flow inside the fracture, s is the curvilinear coordinate along the fracture, q_t and q_b are fluid leak-off into the top and bottom fracture surfaces, respectively.

The tangential flow is governed by the classical cubic law as [39]

$$q = -\frac{w^3}{12\mu} \frac{\partial p_f}{\partial s} \quad (9)$$

where μ is the viscosity of fracturing fluid, which is assumed to be identical to that of pore fluid in this paper; p_f is the fluid pressure in the fracture.

The normal flow (leak-off) across the top and bottom fracture surfaces can be described as

$$\begin{cases} q_t = c_t(p_f - p_t) \\ q_b = c_b(p_f - p_b) \end{cases} \quad (10)$$

where p_t and p_b are the pore fluid pressures in the porous medium adjacent to the top and bottom surfaces of the fracture; c_t and c_b are the parameters controlling the fluid flow across the top and bottom fracture surfaces, usually referred as "leak-off coefficients."

2.2 Boundary conditions and weak forms

Figure 2 shows a porous medium with a hydraulic fracture and the boundary conditions. The essential boundary conditions are described by

$$\begin{cases} u = \bar{u} & \text{on } \Gamma_u \\ p = \bar{p} & \text{on } \Gamma_p \end{cases} \quad (11)$$

where \bar{u} and \bar{p} are prescribed displacement and pore pressure at the external boundaries.

The natural boundary conditions are expressed as

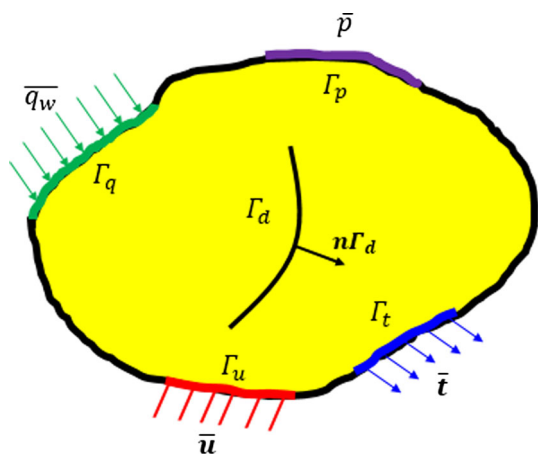


Fig. 2 A porous medium containing a hydraulic fracture subjected to boundary conditions

$$\begin{cases} \sigma \cdot n = \bar{t} & \text{on } \Gamma_t \\ v_d \cdot n = \bar{q}_w & \text{on } \Gamma_q \end{cases} \quad (12)$$

where \bar{t} and \bar{q}_w are prescribed traction and flux on the external boundaries; n is the unit outward normal vector to the external boundaries.

On the surfaces of the fracture, the following boundary conditions are defined

$$\begin{cases} \sigma \cdot n_{\Gamma_d} = t^c - p_f n_{\Gamma_d} \\ \llbracket v_d \rrbracket \cdot n_{\Gamma_d} = q_{wd} \end{cases} \quad (13)$$

where t^c is the cohesive traction (the fracture growth is modeled based on a cohesive law which will be described later); n_{Γ_d} is the unit normal vector to the fracture; q_{wd} is the fluid leak-off flux from the fracture to the formation; and the notation $\llbracket \cdot \rrbracket$ denotes the discrepancy between the values at the two fracture surfaces.

The weak form of the equilibrium equation can be obtained by integrating Eq. 4 with a test function η over the domain Ω :

$$\int_{\Omega} \nabla^s \eta : \sigma d\Omega + \int_{\Gamma_d} \llbracket \eta \rrbracket \cdot (t^c - p_f n_{\Gamma_d}) d\Gamma = 0 \quad (14)$$

where ∇^s is the symmetric part of the gradient operator. Note that the total stress tensor σ in this equation must be replaced by the effective stress tensor in Eq. 5.

The weak form of the continuity equation of pore fluid flow (Eq. 6) can be obtained by multiplying the equation with a test function ζ , substituting the Darcy’s law (Eq. 7), and integrating the equation over the domain:

$$\begin{aligned} & \int_{\Omega} \zeta \left(\frac{1}{M} \dot{p} + \alpha \nabla \cdot \dot{u} \right) d\Omega + \int_{\Omega} \frac{k}{\Omega \mu} \nabla \zeta \cdot \nabla p d\Omega - \int_{\Gamma_d} \zeta q_{wd} d\Gamma \\ & + \int_{\Gamma_p} \zeta \bar{q}_w d\Gamma \\ & = 0 \end{aligned} \quad (15)$$

Similarly, the following weak form of the continuity equation of fracture fluid flow (Eq. 8) can be obtained with a test function ξ :

$$\int_{\Gamma_p} \xi (\dot{w} + q_t + q_b) d\Gamma + \int_{\Gamma_p} \frac{\partial(\xi q)}{\partial s} d\Gamma + \int_{\Gamma_p} \frac{w^3}{12\mu} \frac{\partial p_f}{\partial s} \frac{\partial \xi}{\partial s} d\Gamma = 0 \quad (16)$$

For the hydraulic fracturing problem in a porous medium, the fields we want to solve are the displacement field, the pore pressure field, and the fracture fluid pressure field. The coupling between these variables is embodied in Eqs. 14–16. The pore pressure is coupled with displacement by Eqs. 14 and 15. The pore pressure is coupled with fracture fluid pressure by Eqs. 15 and 16. The fracture pressure is coupled with the displacement field (fracture width) through Eq. 16.

2.3 Finite element approximation and discretization

XFEM is implementation based on the so-called phantom node approach in this paper [33, 40]. Figure 3 illustrates the decomposition of a fractured element into two elements formed by original nodes and additional phantom nodes. The enriched local displacement is defined as

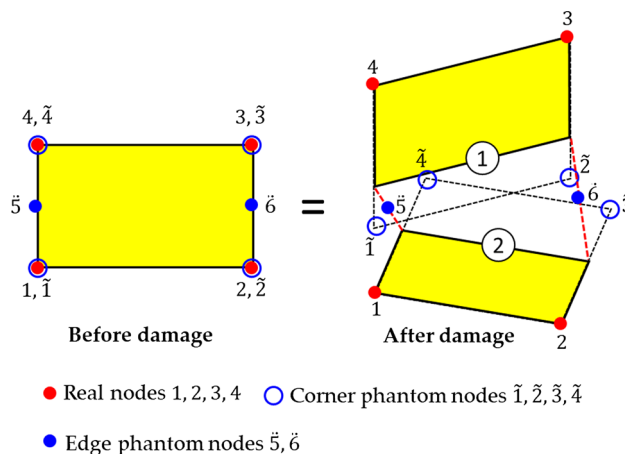


Fig. 3 Schematic of the real and phantom nodes on an enriched element before and after damage

$$\mathbf{u}(\mathbf{x}) = \sum_{i \in S_{\text{all}}} N_i(\mathbf{x}) \mathbf{u}_i + \sum_{j \in S_{\text{frac}}} N_j(\mathbf{x}) [H(f(\mathbf{x})) - H(f(x_j))] \mathbf{a}_j \tag{17}$$

where S_{all} is the set of all nodes; S_{frac} is the nodes set whose support elements are cut by fracture interior; $N_i(\mathbf{x})$ is the standard finite element shape function; \mathbf{u}_i is the usual nodal displacement vector for the continuous part of the finite element solution; $H(x)$ is the enriched function, also called Heaviside function, for the displacement jump across the fracture; and \mathbf{a}_j is the nodal enriched degree of vector for nodes whose shape function support domain is cut by the fracture interior.

The Heaviside function is given by [26]:

$$H(\mathbf{x}) = \begin{cases} 1, & \text{if } (\mathbf{x} - \mathbf{x}^*) \cdot \mathbf{n} \geq 0 \\ -1, & \text{if } (\mathbf{x} - \mathbf{x}^*) \cdot \mathbf{n} < 0 \end{cases} \tag{18}$$

where \mathbf{x} is a sample point; \mathbf{x}^* is the point on the fracture closest to \mathbf{x} ; \mathbf{n} is the unit outward normal to the fracture at \mathbf{x}^* .

For an element cut by a fracture and decomposed into two elements in the phantom node approach (Fig. 3), the displacement field is given as

$$\mathbf{u}(\mathbf{x}, t) = \sum_{i \in S_1} N_i(\mathbf{x}) \mathbf{u}_i^1 H(-f(\mathbf{x})) + \sum_{i \in S_2} N_i(\mathbf{x}) \mathbf{u}_i^2 H(f(\mathbf{x})) \tag{19}$$

where S_i is the node sets of superposed element i ; \mathbf{u}_i^j is the nodal degree of freedom of superposed element j . Each element is formed with both real nodes and phantom nodes as shown in Fig. 3.

Since the fracture does not impose discontinuity in pressure field, the fracture fluid pressure and pore pressure are not enriched. They are approximated with the standard FEM approximation as [44]:

$$p(\mathbf{x}) = \sum_{i \in S_{\text{all}}} N(\mathbf{x}) p_i \tag{19}$$

where p_i is the pore pressure at node i or the fluid pressure in the fracture at phantom node i .

Next, we turn our attention to the discretization of the momentum equation and fluid flow equation. The discrete momentum equation can be obtained by performing FEM discretization of the weak form Eq. 14 as

$$\mathbf{f}^{\text{ext}} = \mathbf{f}^{\text{int}} + \mathbf{f}^{\text{pore}} + \mathbf{f}^{\text{fluid}} + \mathbf{f}^{\text{coh}} \tag{20}$$

where \mathbf{f}^{ext} , \mathbf{f}^{int} , \mathbf{f}^{pore} , $\mathbf{f}^{\text{fluid}}$ and \mathbf{f}^{coh} are the external force, internal force, pore fluid force, fracture fluid force, and cohesive contact force. They are assembled from element matrices and given as follows for an element e that is splitted into a pair of elements (elements 1 and 2 as shown in Fig. 3) [40, 44].

$$\mathbf{f}_{ei}^{\text{ext}} = \int_{\Gamma_i^e} \mathbf{N}^T \bar{\mathbf{t}} H((-1)^i f^e(\mathbf{x})) d\Gamma \tag{21}$$

$$\mathbf{f}_{ei}^{\text{int}} = \int_{\Omega^e} \mathbf{B}^T \boldsymbol{\sigma}_e H((-1)^i f^e(\mathbf{x})) d\Omega \tag{22}$$

$$\mathbf{f}_{ei}^{\text{pore}} = \int_{\Omega^e} \alpha \mathbf{N}^T \frac{\partial p}{\partial \mathbf{x}} H((-1)^i f^e(\mathbf{x})) d\Omega \tag{23}$$

$$\mathbf{f}_{ei}^{\text{fluid}} = (-1)^i \int_{\Gamma_d^e} \mathbf{N}^T p \mathbf{n} d\Gamma \tag{24}$$

$$\mathbf{f}_{ei}^{\text{coh}} = (-1)^i \int_{\Gamma_d^e} \mathbf{N}^T \mathbf{t}^c d\Gamma \tag{25}$$

where the subscript i represents the superposed elements, either 1 or 2 as shown in Fig. 3; \mathbf{N} is the matrix of the finite element shape function; and \mathbf{B} is the discrete strain–displacement operator.

Neglecting the body force of fluid, the discrete form for fluid flow is given by [28, 44]

$$\mathbf{C}\underline{p} + \mathbf{Q}\underline{u} + \mathbf{H}\underline{p} = \mathbf{f}_p^{\text{ext}} \tag{26}$$

where

$$\mathbf{C} = \int_{\Omega} \frac{1}{M} \mathbf{N}^T \mathbf{N} d\Omega \tag{27}$$

$$\mathbf{Q} = \int_{\Omega} \alpha (\nabla \mathbf{N})^T \cdot \mathbf{N} d\Omega \tag{28}$$

$$\mathbf{H} = \int_{\Omega} (\nabla \mathbf{N})^T \cdot \boldsymbol{\kappa} \cdot \nabla \mathbf{N} d\Omega \tag{29}$$

$$\mathbf{f}_p^{\text{ext}} = \int_{\Gamma_q} \mathbf{N}^T \bar{q}_w d\Omega \tag{30}$$

where $\boldsymbol{\kappa}$ is the so-called permeability coefficient of fluid flow.

By solving the discretization Eqs. 20 and 26 together, the strongly coupled problem between porous rock (deformation and pore fluid flow) and fracture evolution (fracture creation and fracture fluid flow) can be solved.

2.4 Abaqus implementation aspects

In order to model hydraulic fractures in porous media using XFEM, the phantom node technique is implemented in Abaqus in conjunction with XFEM. Phantom nodes with displacement and pore pressure degrees of freedom are introduced to the enriched elements to represent the discontinuity of damaged elements. Before an element is cut by a fracture, each phantom node is perfectly constrained to its corresponding real node as shown in Fig. 3. When the element is cut by a fracture, the phantom nodes on the element are activated and the element splits into two elements. Each element is comprised of a combination of

some real nodes and phantom nodes which are no longer tied together and can move independently.

The cohesive segment method (described in next section) is used in conjunction with the phantom node technique to simulate hydraulic fracture growth. The magnitude of the separation is governed by the cohesive law until the cohesive strength of the fractured element becomes zero, after which the phantom and the real nodes move independently. In order to capture fluid pressure (p_f) in the fracture, additional phantom nodes with only fluid pressure degrees of freedom are introduced onto the edges of each enriched element, as shown by the blue solid circles in Fig. 3. The edge phantom nodes are not activated until the edge is cut by a fracture. The pore pressure (p_t and p_b) acting on the top and bottom surfaces of the fracture is interpolated from pore pressure at the real and phantom corner nodes. The difference between p_f and p_t/p_b drives the leak-off of fluid from the fracture to formation.

The system of nonlinear, coupled equations is solved using the Newton–Raphson method. The continuity equation is integrated in time using the backward Euler approximation, which provides unconditional stability. A minimum time step [43], which is helpful to eliminate spurious oscillations, is used to reinforce the integration procedure:

$$\Delta t \geq \frac{\gamma_F}{6Ek} (\Delta h)^2 \quad (31)$$

where Δt is the time increment; γ_F is the specific weight of fluid; E is the elastic modulus of the solid skeleton; and Δh is the typical element size.

2.5 Cohesive zone model

A cohesive zone model is embedded into the enriched elements in the XFEM model to simulate initiation and propagation of fluid-driven fractures and associated fracturing fluid flow and leak-off. The fracturing process is modeled as progressive degradation of cohesive strength of the enriched elements with a traction–separation damage law.

Figure 4 shows the traction–separation law with linear softening used in this study, which is defined by the fracture toughness (area under the traction–separation curve) and the cohesive strength (peak traction value at the traction–separation curve). The law defines damage initiation and evolution in fracturing process. Before damage initiation, the material follows linearly elastic behavior, determined by the stiffness of the material.

Damage initiation refers to the beginning of degradation of the cohesive strength of an enriched element. It occurs when a damage initiation criterion is satisfied. In this study,

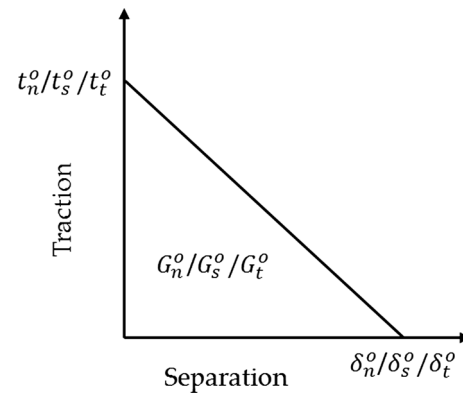


Fig. 4 Traction–separation law with linear softening behavior

the quadratic nominal stress criterion is used to define damage initiation, which can be represented as [38]

$$\left\langle \frac{t_n}{t_n^o} \right\rangle^2 + \left\langle \frac{t_s}{t_s^o} \right\rangle^2 + \left\langle \frac{t_t}{t_t^o} \right\rangle^2 = 1 \quad (32)$$

where t_n , t_s , and t_t are the tractions on the fracture interface in the normal, the first shear, and the second shear directions, respectively. t_n^o , t_s^o , and t_t^o are the cohesive strengths when the deformation is purely normal to the interface (pure tension), purely in the first shear direction, and purely in the second shear direction, respectively. The symbol $\langle \rangle$ represents the Macaulay bracket, used to signify that a pure compressive stress state does not initiate damage at the interface. Note that Eq. 32 is a general equation that includes components on both shear directions. However, in the following section, a 2D model is adopted; thus, only one shear direction component is involved.

Following damage initiation, damage evolution will occur, characterized by a progressive degradation of the cohesive strength. A scalar damage variable D is used to represent the damage of the interface in the numerical model as [38]

$$t_n = \begin{cases} (1-D)T_n, & T_n \geq 0 \\ T_n, & T_n < 0 \end{cases} \quad (33)$$

$$t_s = (1-D)T_s \quad (34)$$

$$t_t = (1-D)T_t \quad (35)$$

where T_n , T_s , and T_t are the normal stress and shear stresses in the first and second shear directions predicted by the elastic traction–separation behavior for the current separations without damage. $t_n = T_n$ when $T_n < 0$ means no damage to pure compressive traction (traction acting normally to fracture faces and against fracture opening). D is the scalar damage variable which has an initial value of 0 and monotonically evolves from 0 to 1 upon further loading from damage initiation to complete failure of the interface. D can be expressed as [10, 42]

$$D = \frac{\delta^f (\delta^{\max} - \delta^0)}{\delta^{\max} (\delta^f - \delta^0)} \quad (36)$$

where δ^f and δ^0 are the effective separation at the complete failure and at the initiation of damage, respectively; δ^{\max} is the maximum effective separation attained during the loading history. The effective separation across the fracture interface with combined normal and shear separations can be defined as:

$$\delta_m = \sqrt{\delta_n^2 + \delta_s^2 + \delta_t^2} \quad (37)$$

where δ_n is the displacement in the normal direction and the Macaulay bracket $\langle \rangle$ means that a pure compressive displacement (induced by pure compressive traction) does not contribute to the effective displacement; δ_s and δ_t are the shear displacements at the first and second shear directions, respectively.

3 Model verification

This section aims to verify the capability of the XFEM-based cohesive segment model on modeling curving hydraulic fractures in the near-wellbore region against published experimental results. To this end, two independent set of experiments on investigating near-wellbore fracture tortuosity reported by [1, 11] are numerically duplicated.

3.1 Verification against Abass et al. [1]

Abass et al. [1] reported a series of experiments to investigate the effect of perforation orientation on near-wellbore fracture tortuosity using cuboid blocks of hydrostone. The dimensions of the blocks are $0.15 \times 0.15 \times 0.25$ m. A vertical wellbore with a radius of 0.01 m was cast in the center of the blocks in the lengthwise direction. The blocks were confined in a triaxial loading vessel with 20,700 kPa vertical, 17,200 kPa maximum horizontal, and 9600 kPa minimum horizontal stresses. The wellbore was perforated along a 0.05-m interval at the middle of the wellbore with a perforation depth of 0.0034 m. Different perforation angles (angle θ between perforation direction and S_H direction, see Fig. 1) from 0° to 90° were utilized in the experiments. The injection fluid had a viscosity of $1.18E-3$ kPa s and was injected at a rate of $1.67E-8$ m³/s to fracture the wellbore. No initial pore pressure was present within the blocks.

For model verification, a 2D plane-strain model is used to model fracture trajectory on the cross section through the center of the perforated interval. Only the case with a 60° perforation angle is modeled because a relatively clear photograph for this case was provided by Abass et al.[1].

The perforations are modeled as prescribed starter fractures on wellbore wall. It should be noted that the wellbore in the experiment was cased and cemented, but no casing or cement is considered in the numerical model. According to a numerical comparison reported by Gordeliy et al. [20], the near-wellbore fracture trajectories in an open hole and cased hole do not have significant difference. The properties of the blocks in the experiments are summarized in Table 1 and used as input parameters for the numerical modeling.

Figure 5a is a photograph of the curving bi-wing fracture observed from the experiment. It can be seen that the fracture reorients to the direction of S_H as it propagate outwards from the wellbore. In order to validate the numerical model, the fracture path in Fig. 5a is digitalized and plotted in Fig. 5b together with the fracture path obtained from the model. Only the path of the upper fracture wing is compared because the two wings are almost symmetric. The comparison indicates that the simulation result matches the experimental result quite well. This agreement demonstrates the capability of the XFEM-based cohesive segment method on modeling non-planar fractures from a wellbore.

3.2 Verification against Chen et al. [11]

To further verify the proposed model, a similar experiment performed by Chen et al. [11] is numerically duplicated as well. This experiment also aims to investigate fracture behaviors in the near-wellbore region from oriented perforations. The dimensions of the cubic blocks used in this experiment are $0.3 \times 0.3 \times 0.3$ m, which are larger than those of Abass et al. [1] and should allow better observation of fracture reorientation. A wellbore with a radius of 0.01 m was cast in the center of the blocks. The wellbore was then cased and perforated along a 0.05-m interval at the wellbore center. The perforations have a depth of 0.03 m and a phasing angle of 180° . A series of perforation orientations with $\theta = 0^\circ, 30^\circ, 45^\circ, 60^\circ,$ and 75° were considered in the experiments. Similarly, only the case

Table 1 Physical and mechanical properties of the rock samples in Abass et al. [1]

Parameters	Values	Units
Young's modulus	1.74×10^7	kPa
Poisson's ratio	0.228	
Fracture toughness	2500	kPa m ^{0.5}
Tensile strength	5560	kPa
Permeability	9.5	mD
Porosity	0.33	

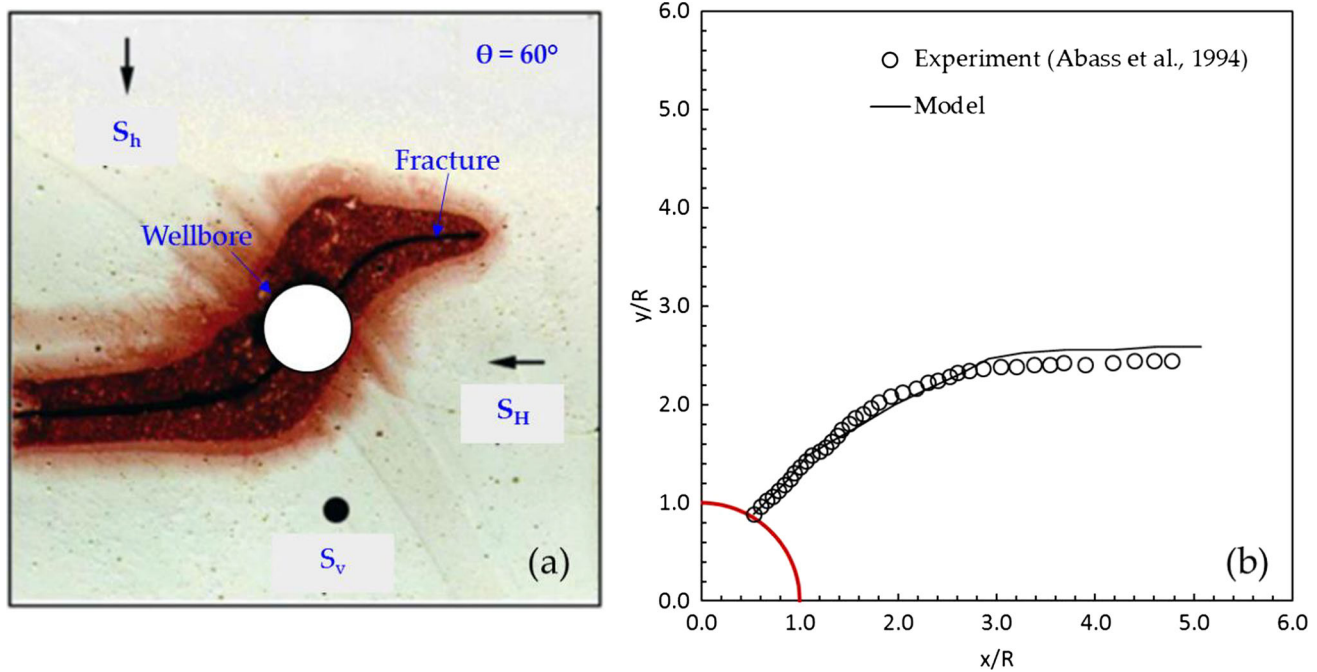


Fig. 5 **a** A photography of the curving bi-wing fracture obtained from the experiment of Abass et al. [1]; **b** comparison of the fracture trajectories obtained from the simulation and digitalized from the photography

with $\theta = 60^\circ$ is simulated for verification purpose and the casing and cement are not explicitly considered. The block was confined in a true triaxial loading vessel and the principal stresses applied were: 15,000 kPa vertical, 6000 kPa maximum horizontal, and 1000 kPa minimum horizontal stresses. Initial pore pressure is also not considered. Fracturing fluid with a viscosity of $1.33\text{E}-4$ kPa·s was injected at an extremely low rate of $2.1\text{E}-9$ m³/s to achieve stable fracture growth. The physical and mechanical properties of the rock samples are summarized in Table 2.

Figure 6a is a photograph provided by Chen et al. [11] showing the curving fracture observed in the experiment. The fracture trajectory is also digitalized and replotted in Fig. 6b to compare with the results from numerical simulation. Because of symmetry, only the trajectory of the

upper fracture wing is compared. Figure 6b shows that there is relatively good agreement between the simulation and experimental results. This comparison result again verifies that the proposed model is a valid tool for predicting near-wellbore fracture complexity.

4 Numerical examples and results

4.1 Model formulation

Single, bi-wing, and multiple fractures initiated from starter fractures on the wellbore wall are considered in this paper. Figure 7 shows the case with a bi-wing starter fracture. The formation is assumed to be an isotropic, poroelastic material in a 2D plane-strain condition. The total domain of the model is 3.2×3.2 m and the wellbore radius is 0.1 m. The number, length, and angle of the starter fractures can vary for different cases. The formation geometry is discretized using enriched XFEM elements with displacement and pore pressure degrees of freedom, which allows arbitrary fracture propagation in the domain.

The wellbore is created by removing a set of elements representing the wellbore. Before elements removal, S_H and S_h are applied, respectively, along the direction of x - and y -axis to each element as the initial stresses, and a uniform initial pore pressure is applied to the whole model as well. The normal displacements at the external boundaries of the model are restricted, and a constant pore

Table 2 Physical and mechanical properties of the rock samples in Chen et al. [11]

Parameters	Values	Units
Young's modulus	8.4×106	kPa
Poisson's ratio	0.23	
Fracture toughness	200	kPa m ^{0.5}
Tensile strength	2590	kPa
Permeability	0.1	mD
Porosity	0.185	

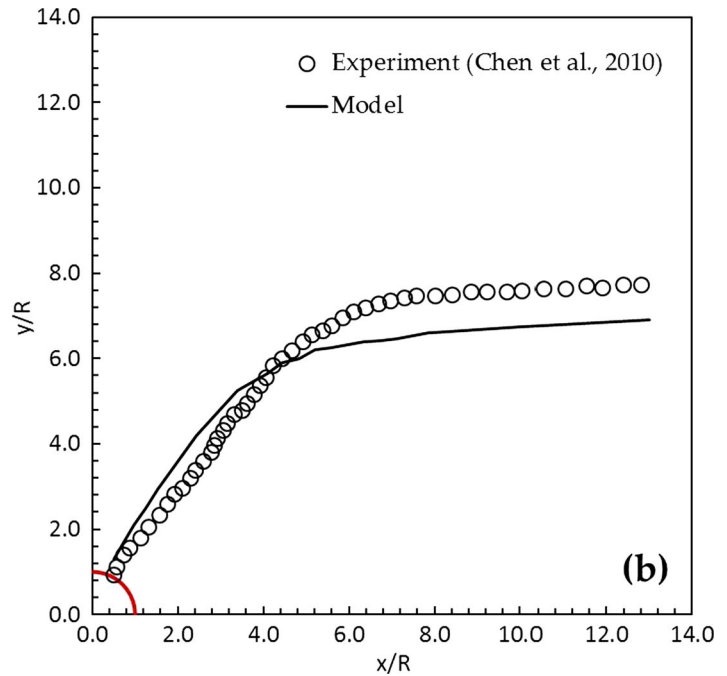
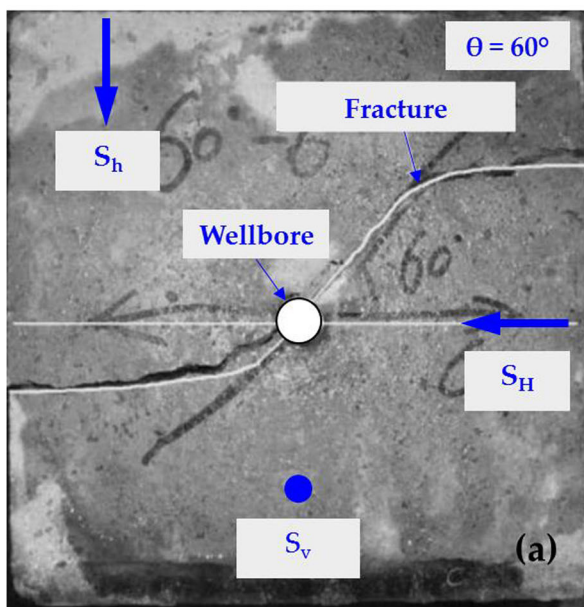


Fig. 6 **a** A photography of the curving fracture trajectory obtained from the experiment of Chen et al. [11]; **b** the trajectories of the upper fracture obtained from the modeling and digitalized from the photography

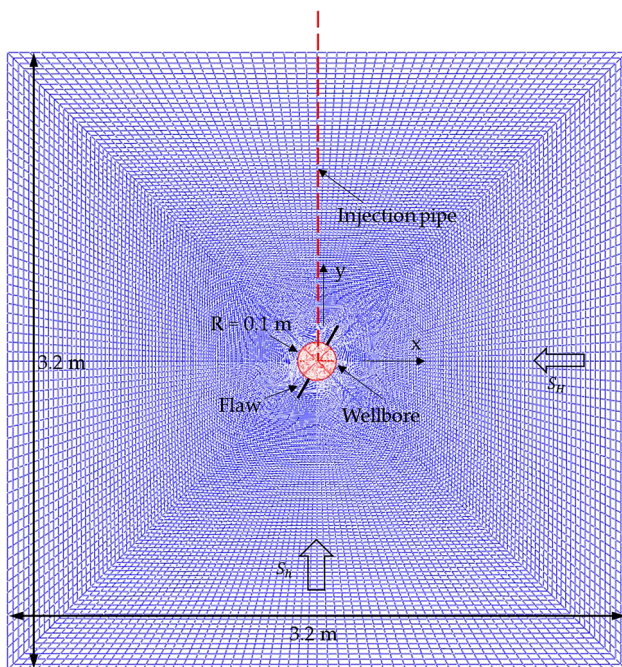


Fig. 7 The geometry and mesh of the near-wellbore hydraulic fracture model

pressure boundary condition is also applied to these boundaries throughout the simulation.

During the simulation, fluid is injected into the wellbore at a constant rate. This is achieved by explicitly modeling the flow in the injection pipe using fluid pipe elements in

Abaqus, as shown in Fig. 7. Fluid pipe elements only have fluid pressure degrees of freedom and allow simulation of both viscous and gravity pressure losses in a pipe or a pipe network. Flow in the pipe elements is expressed based on Bernoulli's equation as [38]:

$$\Delta P - \rho g \Delta Z = C_L \frac{\rho v^2}{2} \tag{38}$$

where ΔP is pressure difference between two points; ΔZ is elevation difference between two points; v is flow velocity in the pipe; ρ is fluid density; g is the gravity acceleration factor; $C_L = \frac{fL}{D_h}$ is friction loss coefficient; L is the pipe length; f is the friction factor; $D_h = \frac{4A}{S}$ is the hydraulic diameter of the pipe; A is the cross-sectional area of the pipe; and S is the wetted perimeter of the pipe. In this study, the fluid pipe elements are only used as an approach to apply dynamic mechanical and pore pressure boundary conditions on wellbore wall and fracture inlets drilling injection; the gravity and viscosity pressure losses along the injection pipe are not the focus.

During the simulation, it is important to properly link the fluid pipe elements to the formation elements to ensure stress equilibrium and fluid continuity between injection pipe and the formation. Basically, two requirements must be satisfied: (1) fluid pressure at the bottom of the injection pipe should be equal to the pore pressure on the wellbore wall (assuming permeable formation), and (2) mechanical pressure applied on the wellbore wall should be equal to the fluid pressure in the injection pipe. These requirements

are achieved by using the “TIE” and “PORMECH” constraints available in Abaqus. The “TIE” constraint links the end node of the injection pipe to the nodes on the wellbore wall and ensures the same pore pressure degrees of the freedom between these nodes, satisfying requirement (1). The “PORMECH” constraint is used to automatically apply the dynamic fluid pressure at the end of the injection pipe onto the wellbore wall as a mechanical surface pressure during injection, satisfying requirement (2). The “TIE” constraint also automatically divides the injection fluid volume into the fractures during the simulations.

The mesh of the model is also shown in Fig. 7. A total number of 28,163 enriched pore pressure/displacement elements are used to discretize the formation, and 20 fluid pipe elements are used to discretize the injection pipe. Although the overall mesh of the formation is already quite fine for accurately capturing the fracture paths, even finer mesh is used in the wellbore vicinity because relatively larger stress, displacement, and pressure gradients are expected in this region.

The formation is modeled as a poroelastic material. The elastic properties consist of Young’s modulus (E) and Poisson’s ratio (ν); the porous properties include porosity (ϕ) and permeability (K). The parameters defining the traction–separation behavior of the formation, as described in Sect. 2.2, include cohesive strength (T_c) and fracture toughness (G_c) of the material. The injection fluid is assumed to be incompressible and has a viscosity of μ . After a fracture opens, the fracture surfaces have a uniform leak-off coefficient c . The formation properties and other input parameters used in the base case for the parametric study later in this paper are reported in Table 3.

The simulation includes three steps. The first step is a “Geostatic” step in Abaqus to achieve stress equilibrium in the formation before the creation of the wellbore. In this step, the fluid pipe elements are disconnected from the formation and no fluid is injected into the pipe. The field stresses, initial pore pressure, and outside boundary

conditions are applied to the model to obtain an initial stress equilibrium. The second step is to create the wellbore. In this step, a group of elements representing the rock inside the wellbore is removed and the injection pipe is connected to the wellbore wall. The third step is the injection step, in which fluid is injected into the pipe with a constant rate to increase the wellbore pressure and extend the fracture from the wellbore to the far field.

A convergence study was conducted for both spatial and time discretization using the base parameters in Table 3. For spatial discretization, the mesh was refined uniformly by applying twice as many as elements in the model and the distribution of tangential stress along x -axis is compared as shown in Fig. 8a. For time discretization, the time increment (0.002 s) in each step is reduced by half and the fracture opening at the tip element of the perforation was compared as shown in Fig. 8b. The results confirm the selection of the mesh size and time increment in this study.

4.2 Results of the base case

The model described above provides a fully coupled way of modeling hydraulic fracture growth in the near-wellbore region. It can capture fracture trajectory, fracture width, injection pressure, distributions of stress and pore pressure around the wellbore and fracture, and pressure distribution in the fracture. Such information is helpful for understanding near-wellbore fracturing mechanisms and optimizations of hydraulic fracturing and wellbore strengthening operations. In this section, simulation results of the base case with input parameters reported in Table 3 are analyzed to illustrate the capabilities of the proposed model.

The base case models the propagation of a single hydraulic fracture initiating from a starter fracture with $\theta = 60^\circ$. Figure 9a shows the final trajectory of the fracture, which hits the outer boundary after 10-s injection. As expected, the fracture reorients to the direction of S_H as it

Table 3 Input parameters for the base case of the near-wellbore hydraulic fracture model

Parameters	Values	Parameters	Values
Model size	3.2×3.2 m	Young’s modulus	6.5E+7 kPa
Wellbore radius	0.1 m	Poisson’s ratio	0.25
Perforation length	0.1 m	Permeability	0.01 mD
Perforation angle	60°	Porosity	0.2
Perforation number	1	Tensile strength	5000 kPa
Minimum horizontal stress	20,000 kPa	Fracture toughness	1350 kPa m ^{0.5}
Maximum horizontal stress	23,000 kPa	Leak-off coefficient	0
Initial pore pressure	10,000 kPa	Injection fluid viscosity	1E–5 kPa s
Injection rate	1E–4 m ³ /s		

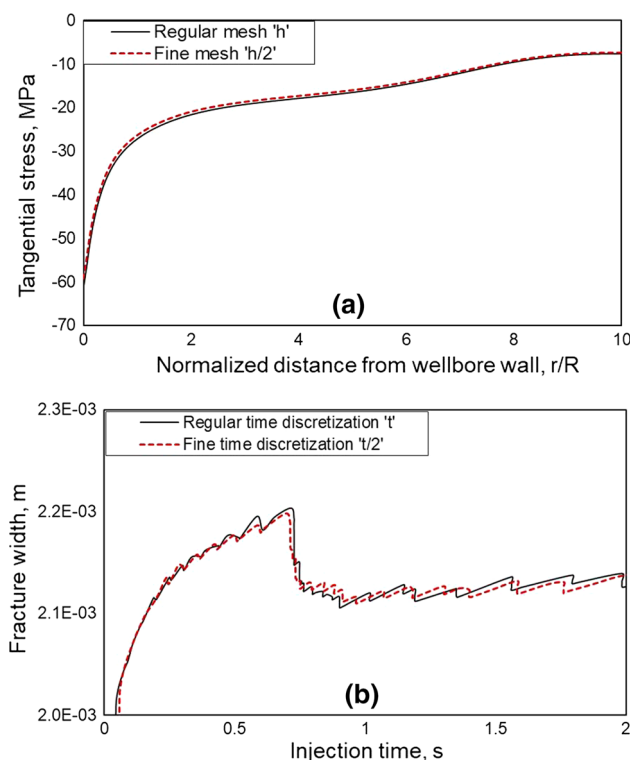


Fig. 8 Convergence studies. **a** Distribution of tangential stress along the direction of x -axis for regular and fine mesh. **b** Fracture width at the perforation tip during injection for regular and fine time discretization

propagates outwards from the wellbore because minimum fracturing resistance exists along this direction. Figure 9b–d shows the distributions of fracture width, fluid pressure, and flow velocity in the fracture at an injection time of 1.6 s. These figures are enlarged views of the area in the red rectangle in Fig. 9a. Figure 9d indicates that the fracture has larger width at its main body while smaller width near the wellbore. This phenomenon was also predicted in the numerical studies of [12, 50], which is believed due to the restriction caused by near-wellbore stress concentration. Near-wellbore fracture tortuosity and width restriction could be beneficial for effectively plugging lost circulation fractures in wellbore strengthening operations, but they could also cause proppant screenout in fracturing stimulation treatments which could be fatal to success of the treatments. Figure 9c shows that fluid pressure decreases along the fracture path due to viscous pressure loss. This demonstrates an improved capability of the proposed model compared with many existing models which assume uniformly distributed internal pressure along the fracture. In this particular case, the pressure drop from fracture inlet to fracture tip is rather small (less than 1 kPa) due to small fracture length and fluid viscosity. Figure 9d shows that the flow velocity also decreases gradually along the fracture

from a maximum value of 0.049 m/s at the fracture inlet to 0 at fracture tip.

Fracture propagation can strongly perturb the stress field around the wellbore. Figure 10 shows minimum principal stress direction around the wellbore before injection and after an injection period of 1.6 s. Figure 10a shows that, before fracture propagation, the minimum principal stress direction is parallel to S_h direction in the far field, indicating the far-field stress field is not perturbed. However, in the near-wellbore region, the minimum principal stresses rotate and become normal to the wellbore wall, indicating the radial stress becomes the least compressive stress. This observation implies that a fracture initiating from a starter fracture not long enough to escape the near-wellbore perturbation region will have a trend to orbit around the wellbore. This possible phenomenon will be further discussed in the following sections. As the fracture propagates away from the wellbore, the stress perturbation area increases as shown in Fig. 10b. Near the wellbore, the minimum principal stress is still normal to the wellbore wall; while around the fracture, the minimum principal stress becomes parallel to the fracture trajectory.

The model can also capture displacement and pore pressure distributions local to the wellbore and fracture during fracture propagation. Figure 11 depicts the results at an injection time of 1.6 s. Figure 11a shows that displacements at two sides of the fracture have opposite directions, but the displacement at the concave side has relatively larger magnitude and has a tendency to rotate to the wellbore, especially in the area close to the wellbore. Figure 11b shows that high pore pressure exhibits around the wellbore and main body of the fracture. Because the permeability in this case is relatively small and the injection time is very short, pore pressure increase in these areas is due to displacement-induced rock compression. Compared with Fig. 11a, it can be seen that the high pore pressure zone is roughly coincident with the area of large displacement. There is a small region ahead of the fracture tip with reduced pore pressure, which is consistent with the simulation studies of other researchers [21, 48]. This low-pressure zone can be explained by rock dilation ahead of the fracture tip during fracture propagation [54].

Time evolutions of displacement (u_{yy}) and effective stress (σ_{yy}) at y -direction on a node A close to the fracture are further investigated (see Fig. 12). At this point, the y -direction is approximately normal to the fracture. It should be noted that the sign of u_{yy} is related to the coordinate direction, i.e., u_{yy} is positive if the displacement is along the positive direction of y -axis and vice versa. Figure 12 shows that, before the fracture tip approaches node A (before 0.6 s), σ_{yy} is approximately equal to the effective minimum horizontal stress of -1.0×10^4 kPa and u_{yy} is

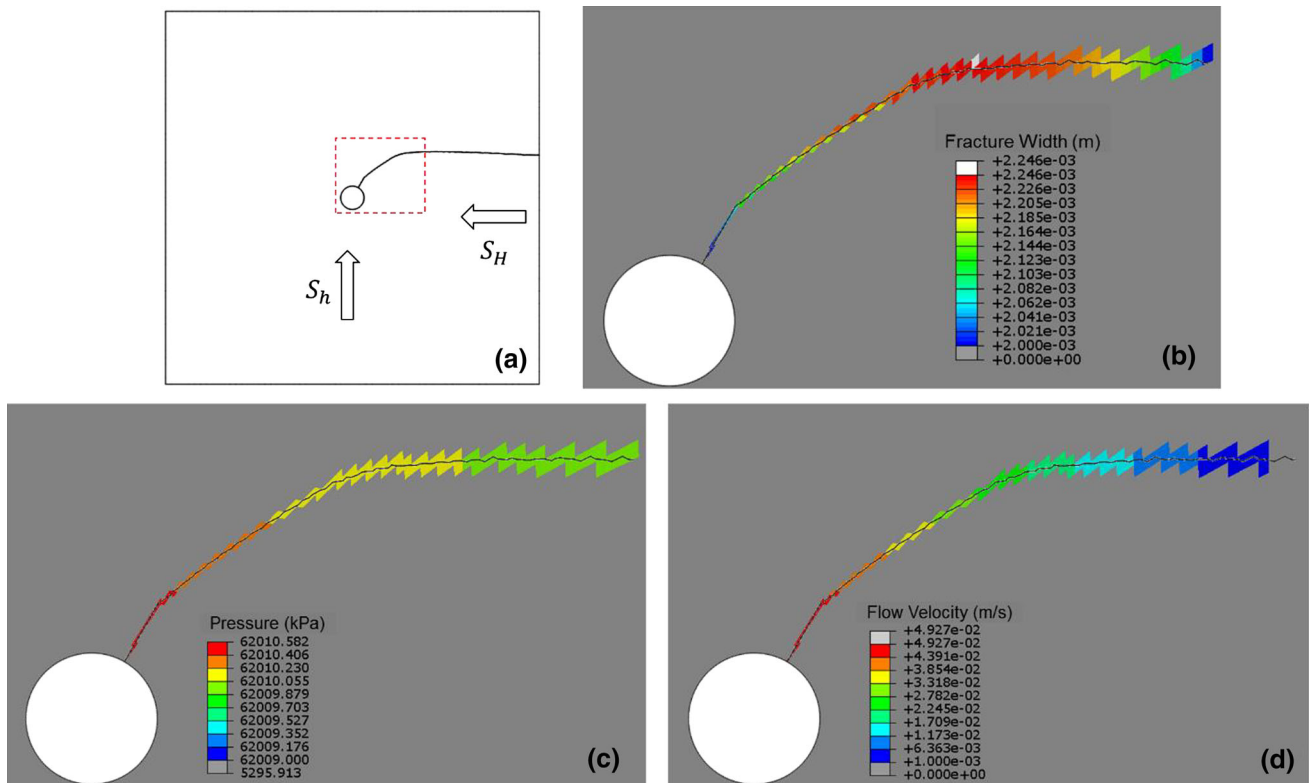


Fig. 9 Final fracture trajectory (a), distributions of fracture width (b), fluid pressure (c), and fluid flow velocity (d) in the fracture at an injection time of 1.6 s. **b–d** Enlarged views of the area in the red rectangle in (a)

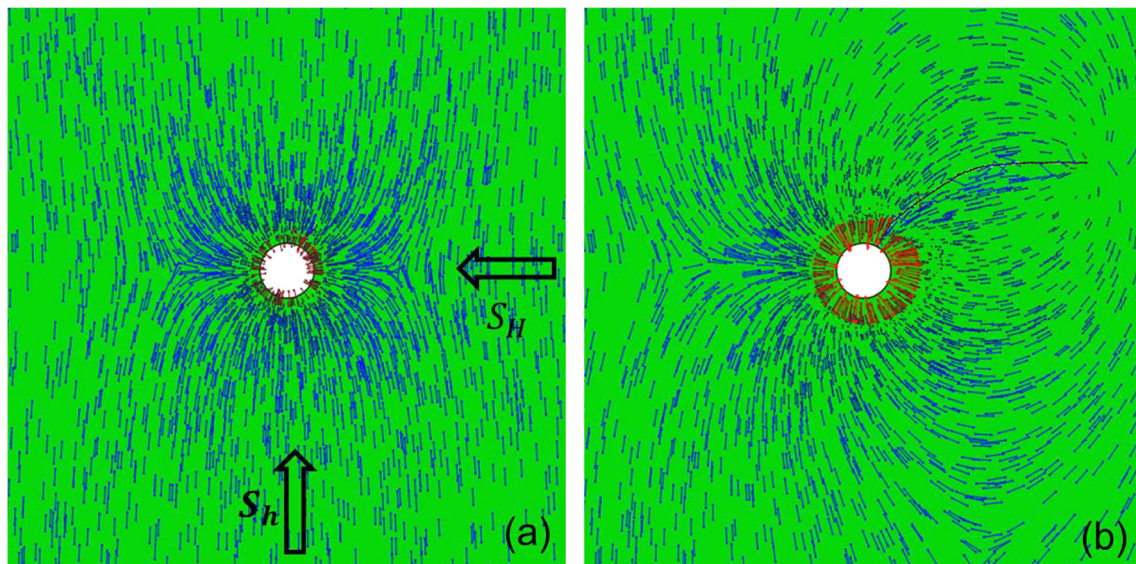


Fig. 10 Direction of minimum principal stress before injection (a) and after an injection period of 1.6 s (b)

roughly equal to zero, indicating the fracture has not influenced this point. When the fracture tip approaches node A, σ_{yy} decreases (i.e., becomes less compressive) due to the dilation ahead of the fracture tip and, meanwhile, there is a small negative displacement at point A. When the fracture tip has passed point A (after 1.5 s), u_{yy} increases

due to the continuous increase in the fracture width while σ_{yy} maintains a relatively constant level. However, clear fluctuations on σ_{yy} and u_{yy} are observed, implying that the fracture propagates intermittently rather than smoothly. Taking the injection interval from 3 to 3.5 s for example, the curve indicates that u_{yy} gradually increases and σ_{yy}

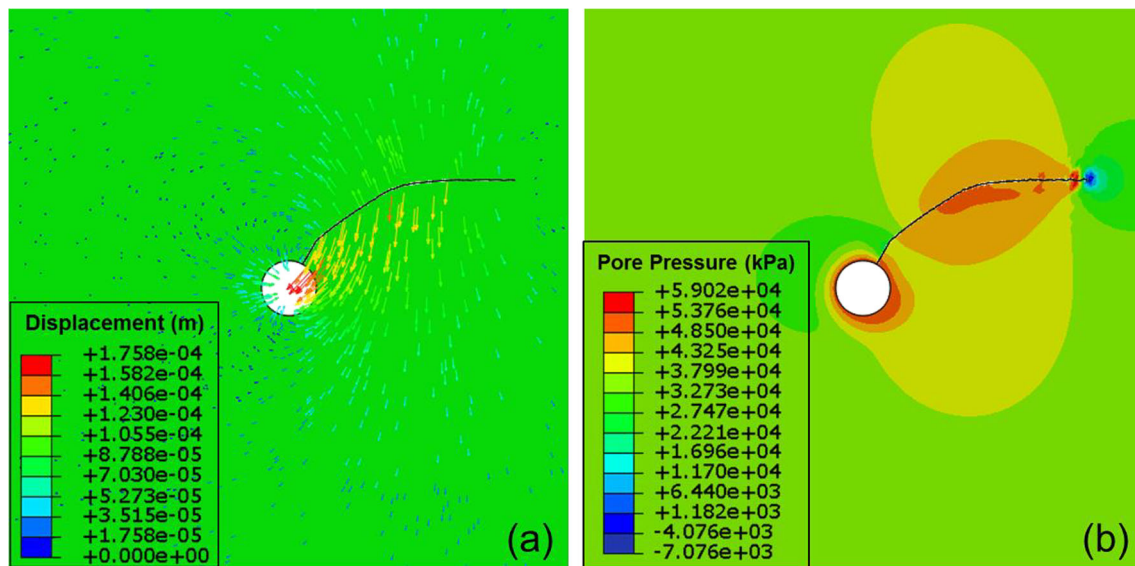


Fig. 11 Displacement (a) and pore pressure (b) in the rock at an injection time of 1.6 s

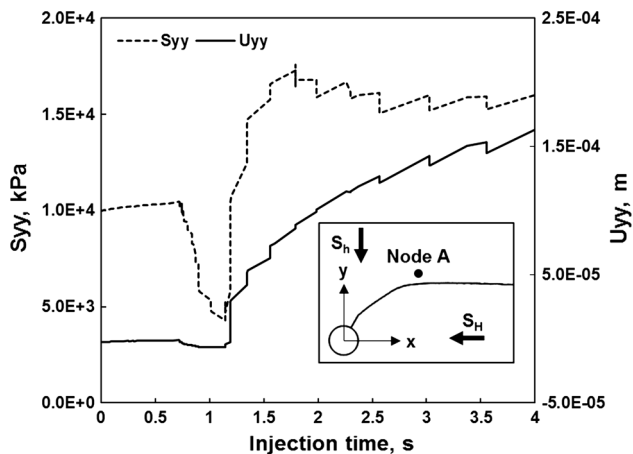


Fig. 12 Vertical stress and displacement at node A close to the fracture

becomes more compressive before 3.5 s, resulting from pressure buildup in the fracture and the corresponding fracture width increase (the fracture tip does not advance during this period). However, at 3.5 s, there exhibits a sudden decline in u_{yy} and elevation in σ_{yy} , implying the fracture tip has a sudden advancement which leads to an immediate decrease in fracture width and relaxation of the compressive stress near the fracture. The pressure buildup and tip advancement will repeat during the entire fracture propagation process.

4.3 Analysis of influential factors

Most previous studies of near-wellbore hydraulic fracturing focus on the impacts of operational factors (e.g., injection rate and fluid viscosity) on near-wellbore fracture

tortuosity. In this section, the parametric study mainly focuses on the effects of the following parameters: porous properties of the rock (i.e., permeability and leak-off coefficient), initial loading conditions (i.e., horizontal stress anisotropy and pore pressure), elastic properties of the rock (i.e., Young's modulus and Poisson's ratio), and strength properties of the rock (e.g., cohesive strength and fracture toughness). The results are analyzed in terms of fracture trajectory, injection pressure, and fracture width. In each sensitivity analysis, only the investigated parameter is changed while all the other parameters are kept the same as those used in the base case (Table 3).

4.3.1 Influence of permeability

Permeability as an important porous property of the rock can significantly affect fluid flow and pore pressure distribution in the wellbore vicinity and consequently influence near-wellbore fracture evolution. Figure 13a depicts fracture trajectories for different permeabilities. The results show that a high permeability can lead to sharper fracture turning. Although all the fractures eventually reorient to the direction parallel to S_H , fractures with higher permeability have a tendency to orbit around the wellbore at early time. This can be explained by the fact that the minimum principal stress around the wellbore at the early time is the radial stress and, therefore, the fracture tends to propagate around the wellbore before it escapes the near-wellbore stress perturbation region. High permeability can cause pore pressure increase around the wellbore which decreases the minimum principal stress in the radial direction and further facilitates fracture orbiting.

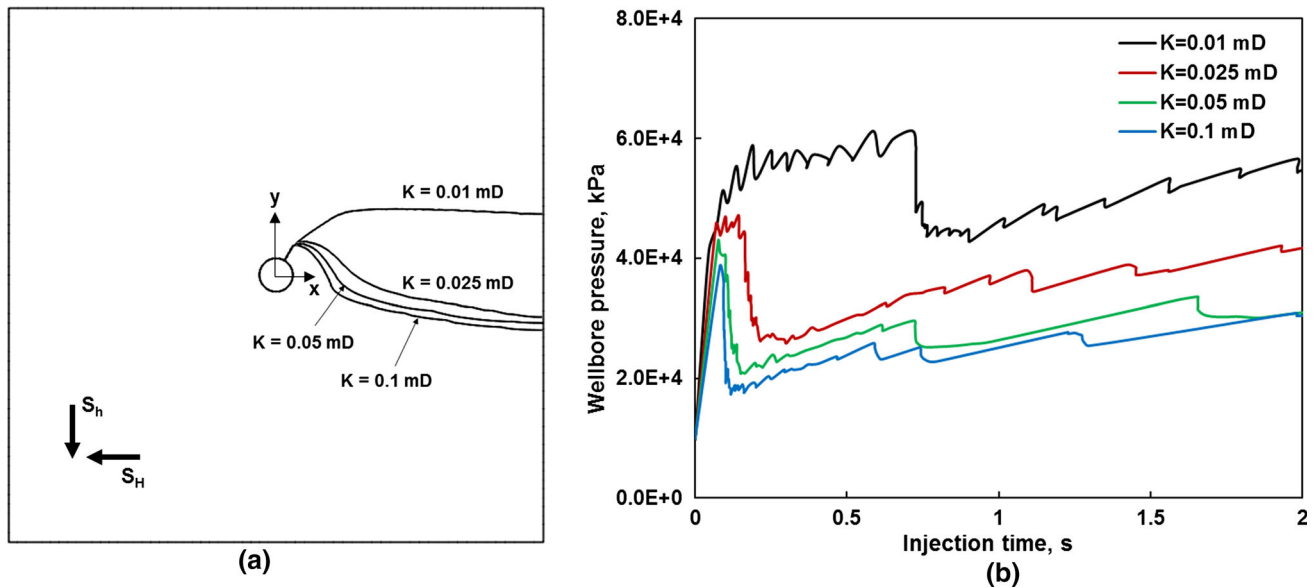


Fig. 13 **a** Fracture trajectories for different permeabilities; **b** wellbore pressure versus time for fracture trajectories in (a)

Figure 13 shows the wellbore pressure during injection for different permeabilities. The results indicate that sharper fracture turning results in lower breakdown pressure and injection pressure profile. Similar simulation results were also reported by Zhang et al. [52]. This is because the confining stress resisting fracture opening is smaller along the sharper turning fracture path in the near-wellbore region; while in the region far away from the wellbore, the confining stress is approximately the same for different fractures and equal to S_h . Figure 13 indicates that the near-wellbore confining stress still influences the injection pressure even though the fracture has propagated far away from the wellbore. Although sharper fracture turning may result in lower breakdown pressure while injecting clean fluid as shown in this study, it may significantly limit transportation of particles in the fracture (e.g., proppant and lost circulation materials) and eventually cause screenout and rapid rise in injection pressure. Figure 14 displays fracture width distributions for different permeabilities at an injection time of 1.6 s. Similarly to the base case, near-wellbore fracture widths in all these cases are restricted. Fracture widths at the main body of the fracture decrease with the increase in permeability, possibly due to the smaller driving pressure in the fracture as shown in Fig. 13b.

4.3.2 Influence of leak-off coefficient

It is well known that fluid leak-off from fracture surfaces to surrounding rock also influences hydraulic fracture behaviors. However, to the authors' knowledge, no previous studies have investigated its impact on near-wellbore

fracture complexity. Figure 15a shows paths for fractures with different leak-off coefficients. In this study, it is assumed that the leak-off coefficient is constant and independent of fluid pressure along the fracture. The base case with zero leak-off is also included in Fig. 15a for reference. The results show that the fracture with a very small leak-off coefficient of $1E-11$ m/s/kPa almost overlaps with the based fracture with zero leak-off, and a larger leak-off coefficient leads to a sharper fracture curving near the wellbore. This observation can be explained by fact that larger leak-off results in reduced minimum principal stress local to the fracture and wellbore which is in the radial direction and, therefore, facilitates fracture turning around the wellbore.

The wellbore pressure versus injection time relationships for fracture paths in Fig. 15a are displayed in Fig. 15b. Similarly to above analysis, the results also show that a sharper fracture turning results in a lower injection pressure profile. Figure 15c shows the development of fracture width at the end of the starter fracture. The fracture width first increases and then decreases as the fracture escapes the near-wellbore region and reorients to the favorable direction. A larger leak-off coefficient leads to a smaller fracture width.

4.3.3 Influence of field stress anisotropy

Field stress anisotropy, i.e., S_H/S_h , can strongly affect near-wellbore stress state and thus local fracture complexity. Figure 16a shows fracture trajectories for different stress anisotropies which are obtained by varying S_H while keeping S_h constant at 20,000 kPa. As expected, larger

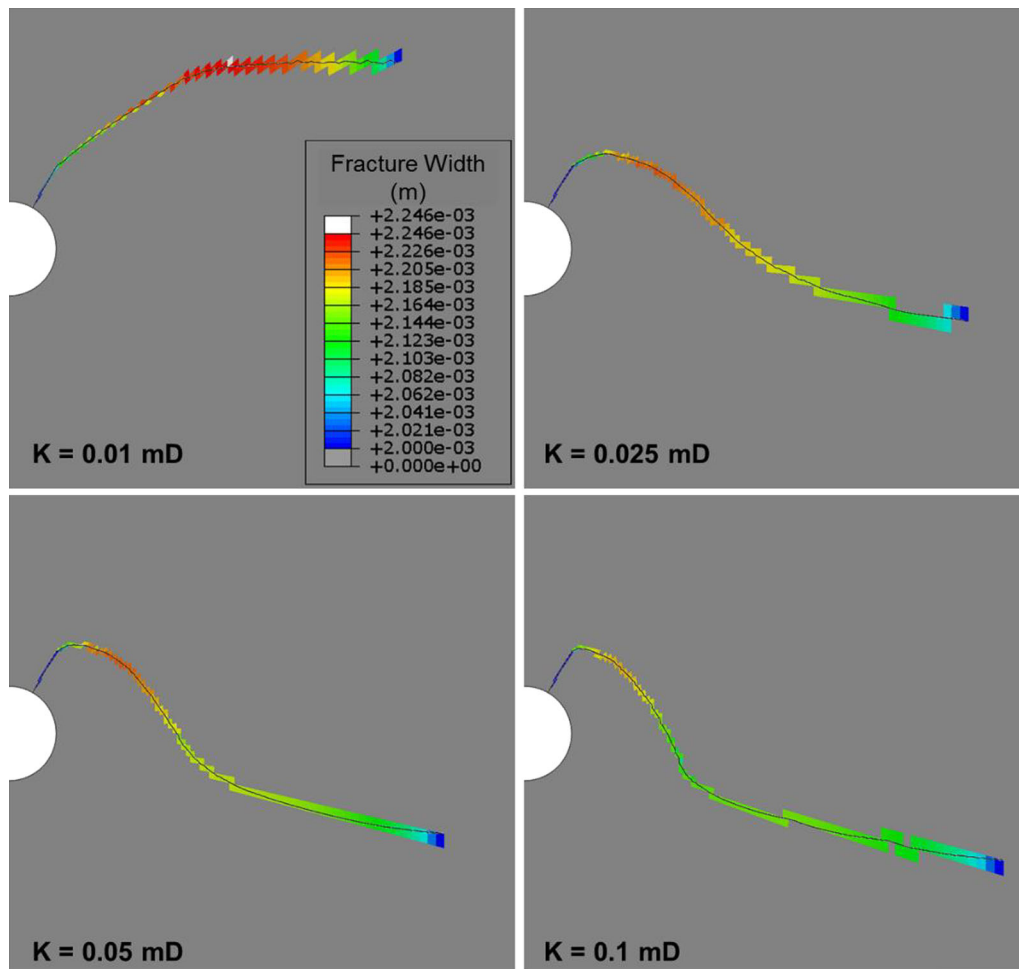


Fig. 14 Fracture width distributions for different permeabilities at an injection time of 1.6 s

stress anisotropy results in sharper fracture turning. When S_H/S_h is reduced to 1.05, the fracture is not able to reorient to S_H direction in the simulated domain. However, if the starter fracture is assigned exactly along S_H direction (not included in the figure), the fracture will propagate without any tortuosity, in agreement with the consensus in hydraulic fracturing community that using oriented perforations in S_H direction can effectively reduce premature screenout.

Figure 16b displays the evolution of wellbore pressure with injection time. It can be seen that a larger horizontal stress anisotropy results in a higher breakdown pressure in this particular case with the starter fracture oriented at 60° . This result seems contradictory to the situation with a starter fracture oriented at 0° (along x -axis), when the breakdown pressure will decrease with the increase in stress anisotropy. This is because, in the near-wellbore region, increased stress anisotropy will lead to decreased hoop stress and hence decreased breakdown pressure at 0° direction, but it will result in increased hoop stress and breakdown pressure at 60° direction. When the fractures

propagate away from the wellbore, the wellbore pressures of the three cases become similar.

4.3.4 Influence of pore pressure

Besides horizontal stresses, pore pressure is another in situ loading factor that can influence near-wellbore fracture behaviors. Figure 17a shows fracture trajectories with different pore pressure but constant S_h (20,000 kPa) and S_H (25,000 kPa). The results indicate that higher pore pressure results in sharper fracture curving in the near-wellbore region, implying that fracturing stimulations in high-pressure reservoirs may create more complex near-wellbore fractures compared with pressure depleted reservoirs. Figure 17b displays the evolution of wellbore pressure with time for fracture trajectories in Fig. 17a. Similar breakdown pressure is observed for the cases with different pore pressure but the same far-field stresses. However, wellbore pressure maintains at a high level for a longer time for the cases with smaller pore pressure because of the corresponding slower fracture turning.

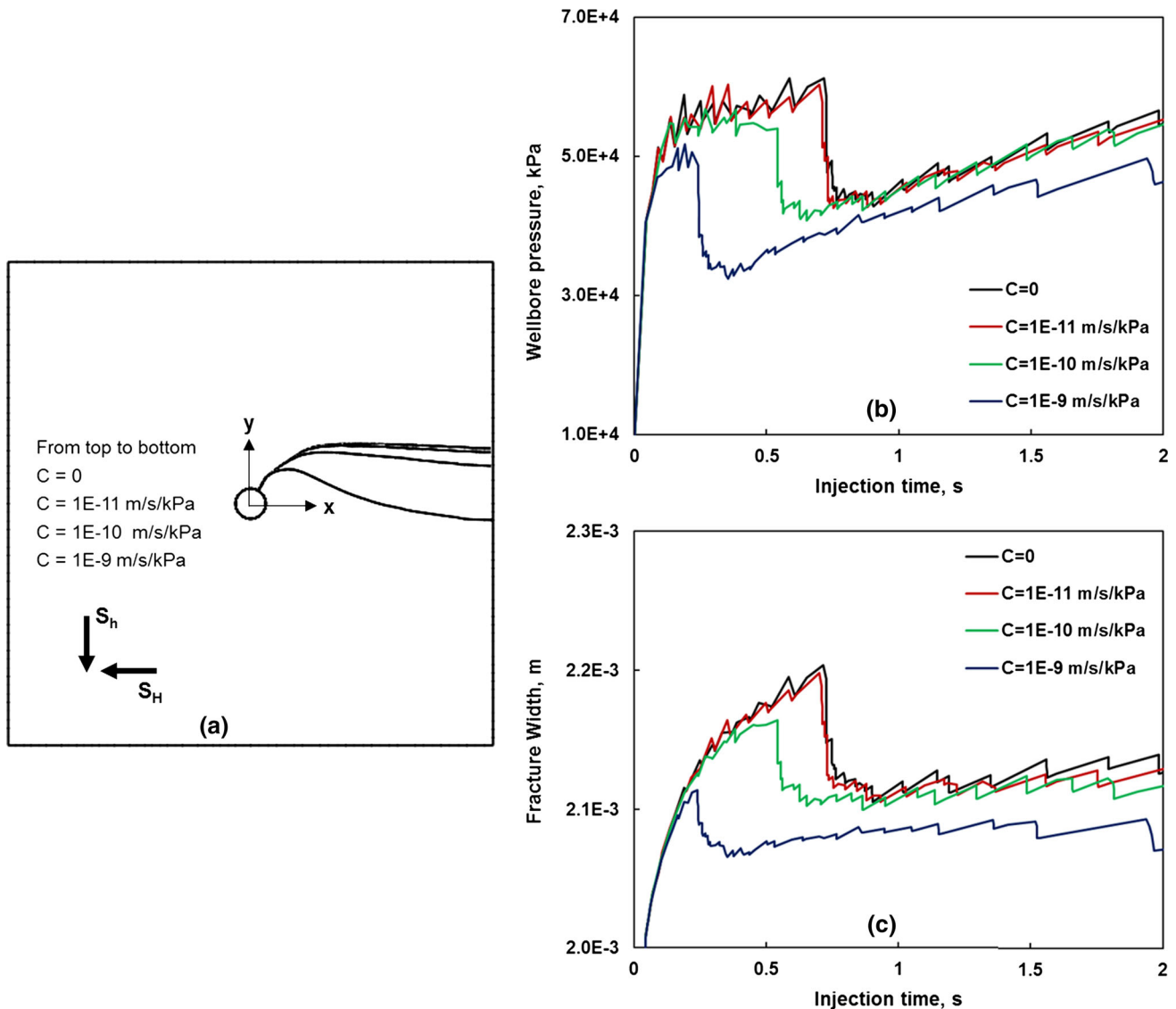


Fig. 15 Fracture trajectories (a), evolution of wellbore pressure (b), and evolution of fracture width at the end of the starter fracture (c) for different leak-off coefficients

4.3.5 Influence of Young's modulus

Young's modulus is an important elastic property for any fracturing simulation studies. However, to the authors' knowledge, no previous studies have investigated its influence on near-wellbore fracture tortuosity. But, according to the fracture-curving coefficient χ_F (Eq. 2) for linearly elastic rocks provided by [22], a larger Young's modulus should lead to a stronger fracture curvature if the fracture growth is viscosity dominated. The fractures for the three cases in Fig. 18 with Young's moduli of $6.5E+7$, $4.0E+7$, and $2.0E+7$ kPa are in viscosity-dominated regime if determined using the dimensionless toughness (Eq. 3). However, simulation results herein for poroelastic rocks indicate that the fracture trajectory is independent of

Young's modulus, as shown in Fig. 18. But Young's modulus can influence fracture propagation speed: Figs. 18a–c clearly show that a larger Young's modulus results in a larger fracture length after the same injection period of 1.6 s. At the end of the injection (10 s), the fractures with relatively larger Young's moduli of $6.5E+7$ and $4.0E+7$ kPa extend to the boundary of the model, while the fracture with a lower modulus of $2.0E+7$ kPa doesn't. This is because the fracture has a smaller width in the rock with a larger Young's modulus (Fig. 19b) and, consequently, creates a larger length with the same amount of fluid injected into the wellbore. Figure 19a shows that a smaller Young's modulus results in a lower wellbore pressure profile, especially after the fracture escapes the near-wellbore stress perturbation region.

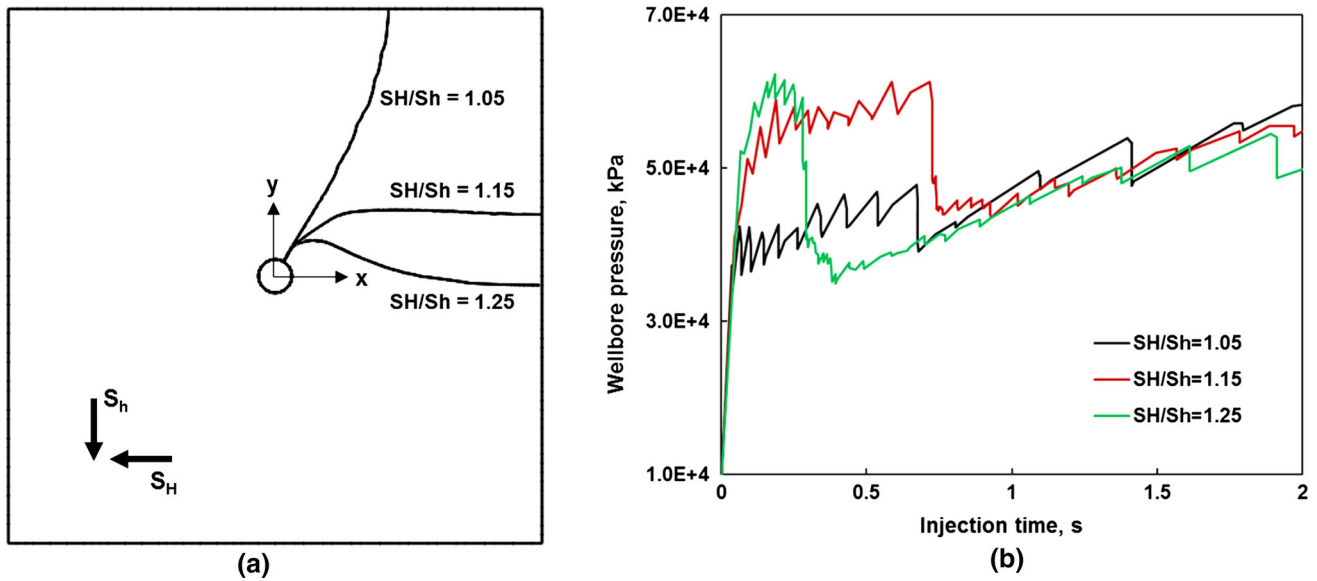


Fig. 16 a Fracture trajectories for different horizontal stress anisotropies; b wellbore pressure versus time for fracture trajectories in (a)

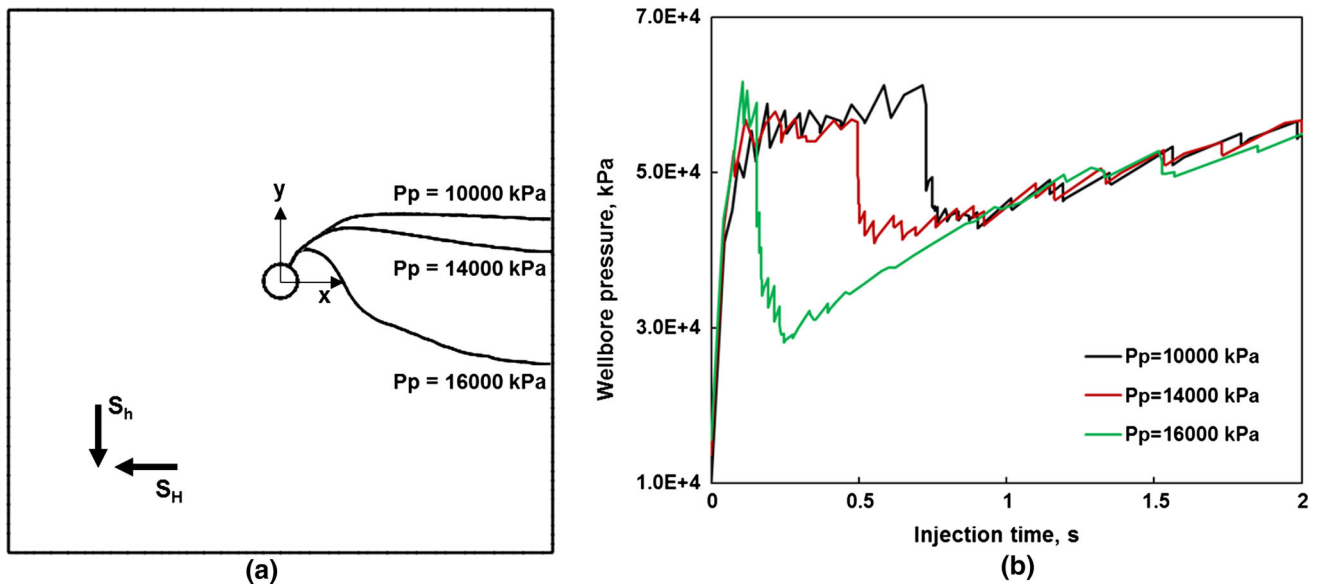


Fig. 17 a Fracture trajectories for different pore pressure; b wellbore pressure versus time for fracture trajectories in (a)

4.3.6 Influence of Poisson’s ratio

Although the fracture path is independent of Young’s modulus, it can be affected by another elastic parameter—Poisson’s ratio. Figure 20a shows that a larger Poisson’s ratio leads to faster fracture turning, which can also be identified by the injection pressure behaviors in Fig. 20b. Different from Young’s modulus which has clear influence on the eventual injection pressure and fracture width, Poisson’s ratio seems not to affect the injection pressure and fracture width after the fracture propagates beyond the near-wellbore region, as shown in Fig. 20b, c.

4.3.7 Influence of cohesive strength

Cohesive strength defines the initiation of material damage in the cohesive zone model as described in Sect. 2.2. Figure 21a shows that the fracture has a larger resistance to reorientation with a larger cohesive strength. Figure 21b indicates that a larger cohesive strength results in a higher injection pressure profile because the fracture is more difficult to initiate. Figure 21c shows that the fracture width at the end of the starter fracture builds up to a larger value with a larger cohesive strength, but it will decline sharply when the fracture extends beyond the near-wellbore region.

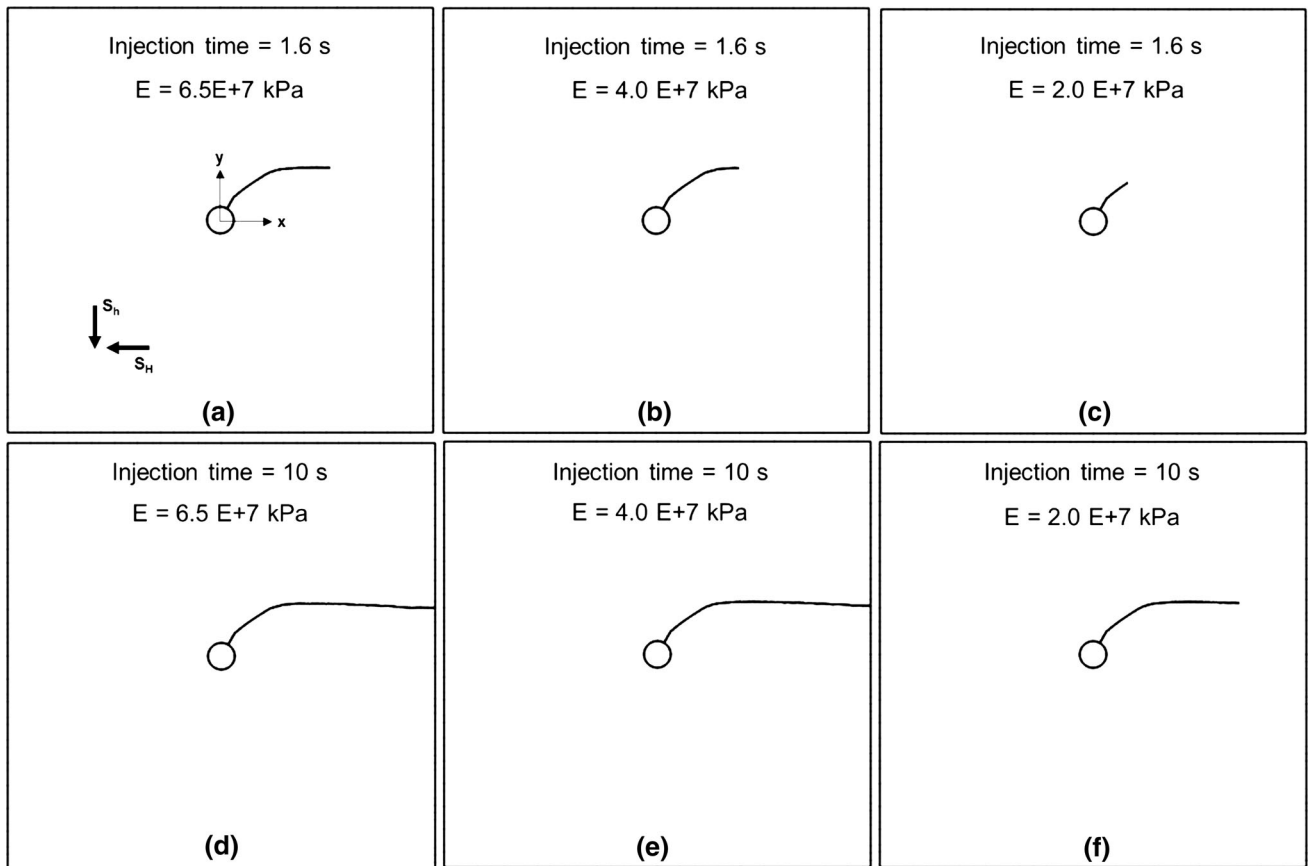


Fig. 18 Fracture trajectories for different Young’s moduli at injection time of 1.6 and 10 s

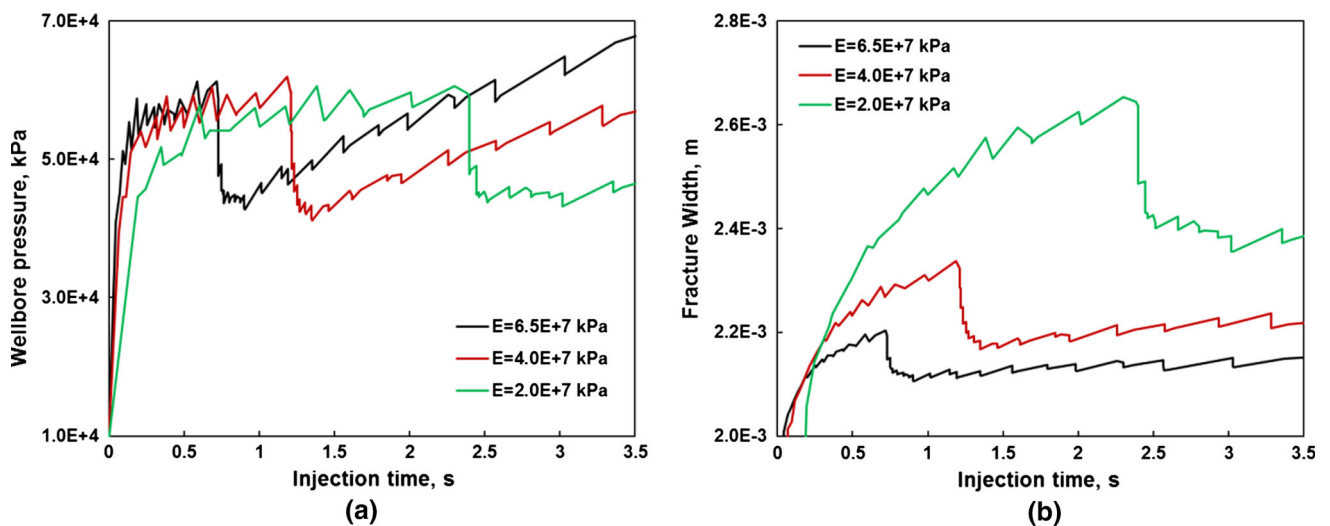


Fig. 19 Evolutions of wellbore pressure (a) and fracture width at the end of the starter fracture (b) with injection time

4.3.8 Influence of fracture toughness

Fracture toughness of sedimentary rocks usually ranges between 1000 and 5000 kPa m^{0.5}. Within this small range, Fig. 22 shows that fracture toughness has negligibly small

influence on near-wellbore fracture trajectory as well as the evolutions of injection pressure and fracture width at the end of the starter fracture in this particular case.

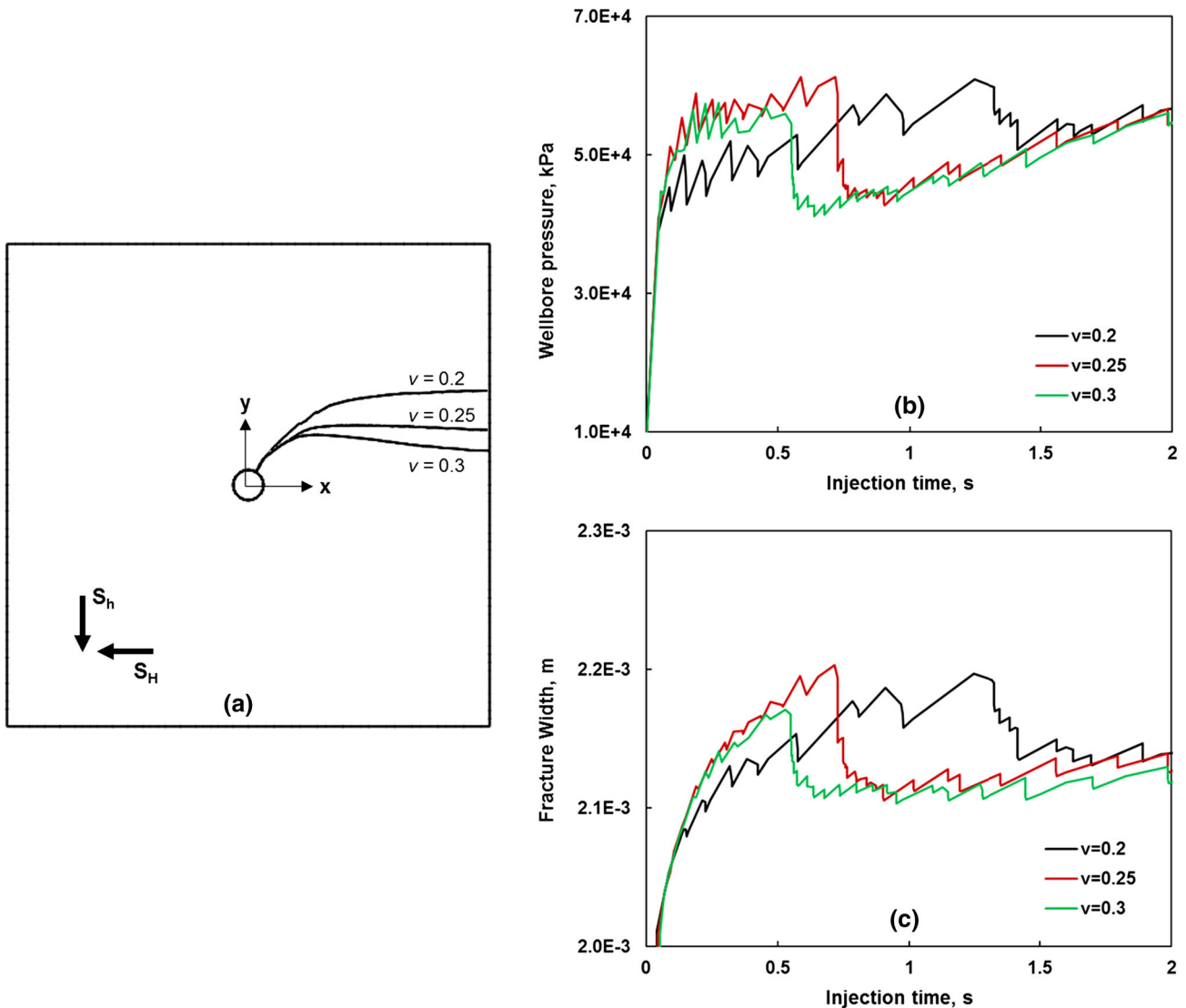


Fig. 20 Fracture trajectories (a), evolution of wellbore pressure (b), and evolution of fracture width at the end of the starter fracture (c) for different Poisson's ratios

4.4 Multiple competing fractures

The proposed model can also be used to simulate propagation of multiple fractures from the wellbore. Figure 23b, c shows the fractures initiating from two starter fractures on the wellbore wall. One starter fracture is fixed at an orientation angle of 60° , while the other orients at 0° , 30° , and the bi-wing (240°) direction. The case with a single starter fracture at 60° (Fig. 23a) is also included for comparison purpose. All the cases have the same injection rate. Figure 23b shows that the bi-wing fractures have stronger curving compared with the single fracture. This is due to the more complex interactions between the fractures and the wellbore, and the reduced flow rate into each fracture wing compared with the single fracture, as it has been well

demonstrated that a lower injection rate can increase the near-wellbore fracture tortuosity.

The two fractures will extend equally when the two starter fractures are located symmetrically with a bi-wing pattern (Fig. 23b). However, if the starter fractures are not bi-wing, there may be only one dominating fracture while the growth of the other fracture is suppressed, such as the cases in Figs. 23c and 22d. In Fig. 23c, the two starter fractures are very close. Before injection, the hoop stress normal to the fracture is smaller for the 30° starter fracture compared with the 60° starter fracture. Therefore, the 30° starter fracture will extend first. With the growth of the 30° starter fracture, the hoop stress around the wellbore, especially in the area close to the fracture, will be elevated. So the growth of the 60° starter fracture is further restricted and stops after a very short time. The two starter fractures

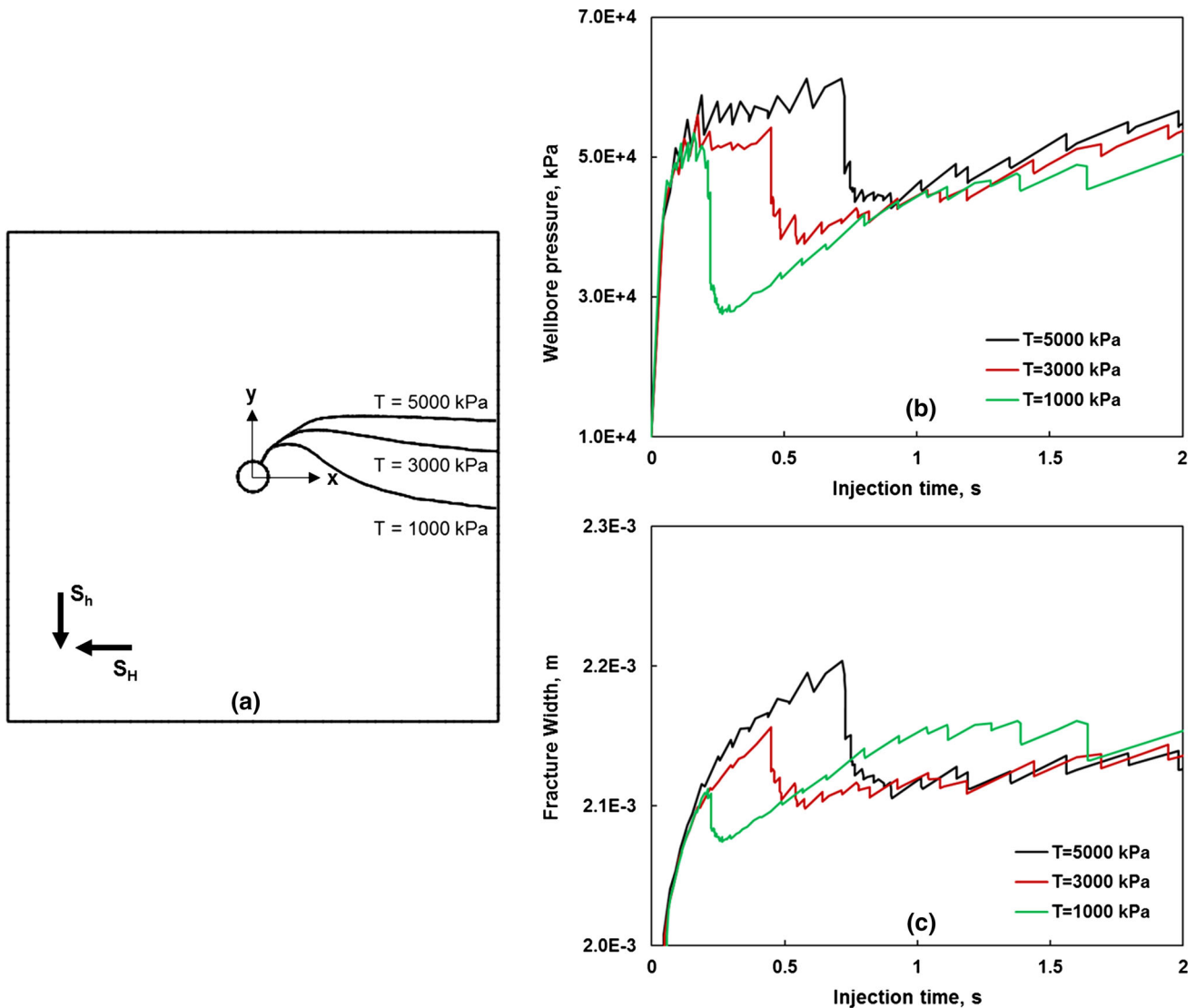


Fig. 21 Fracture trajectories (a), evolution of wellbore pressure (b), and evolution of fracture width at the end of the starter fracture (c) for different cohesive strength

positioned at 0° and 60° in Fig. 23d are relatively further away from each other compared with the fractures in Fig. 23c. Similarly, because of the lower hoop stress at smaller angle to S_H direction, the 0° fracture will propagate first. However, due to the relatively larger distance between the two fractures and thus the relatively smaller stress interference, the 60° starter fracture in this case also propagates, but it bends to and eventually links up with the 0° fracture. This result is qualitatively consistent with the statement of [36] that fracture initiated from perforations at close angles may link up and form one fracture which would be in the direction of the less deviated perforation. Although the 60° fracture only propagates a short distance, the stress interference between the two fractures causes the extension of the 0° fracture not exactly aligned with the direction of S_H .

Figure 24 shows fracture trajectories of two cases with three starter fractures phasing 120° on the wellbore wall. In Fig. 24a, the 0° starter fracture propagates completely. However, for the 120° and 240° starter fractures, although they are located symmetrically with respect to x -axis, only the 120° fracture has complete propagation while the 240° fracture terminates prematurely after a very short extension. In Fig. 24b with starter fractures positioned at 30° , 150° , and 270° , the fracture perpendicular to S_H does not propagate while the other two fractures have full propagation. These results in Fig. 24a, b imply the existence of stress interferences between multiple fractures and non-uniform partition of the injection fluid into the wellbore, which always prefers to flow into fractures with less propagation resistance.

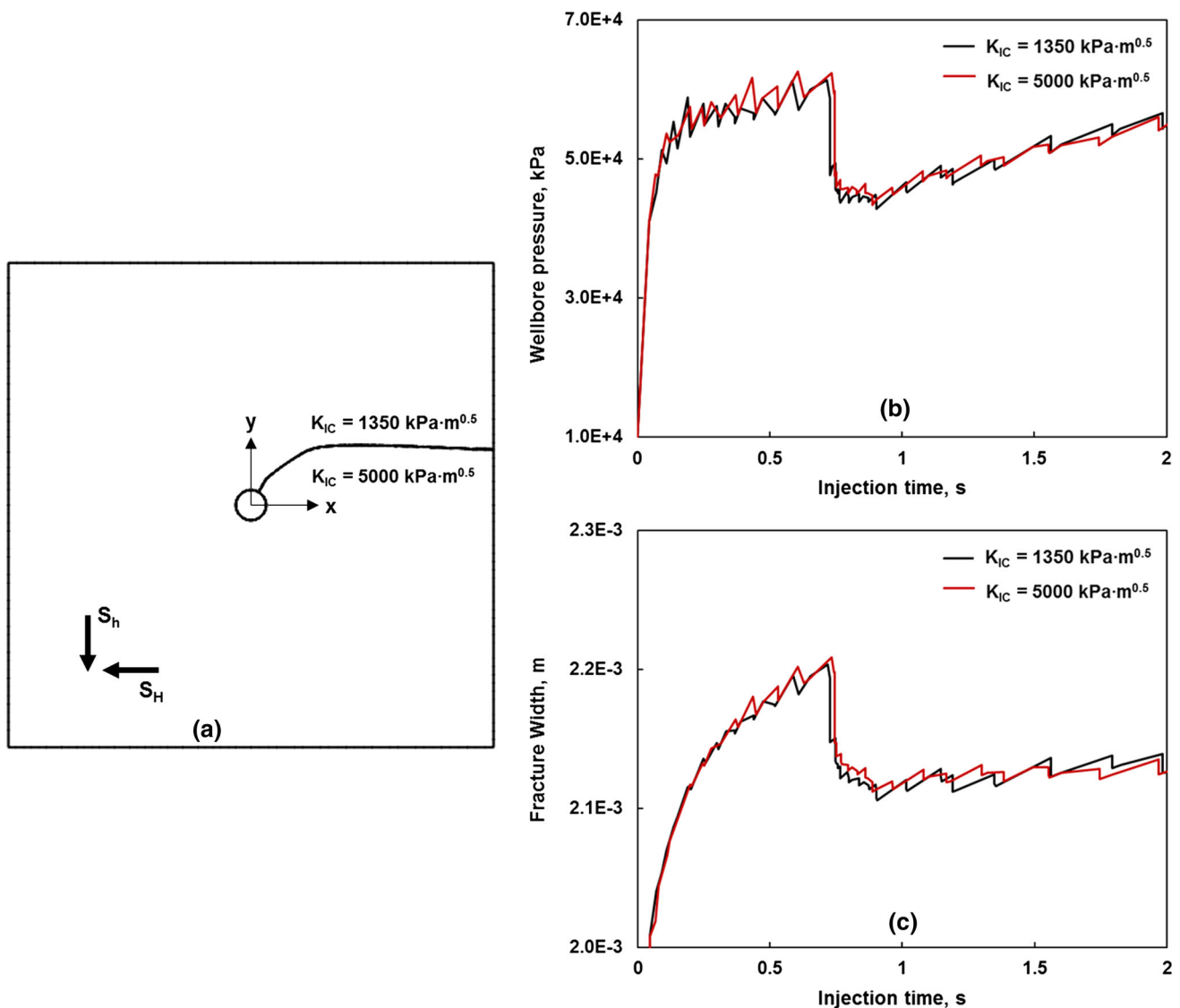


Fig. 22 Fracture trajectories (a), evolution of wellbore pressure (b), and evolution of fracture width at the end of the starter fracture (c) for different fracture toughness

5 Discussions and implications for petroleum engineering

An optimal hydraulic fracturing treatment would generate a single bi-wing fracture with minimum tortuosity at an achievable breakdown pressure [8]. The near-wellbore fracture complexities should be avoided as much as possible. The same requirement is also desirable in some other fracturing-related injection operations, such as field injectivity tests, CO_2 injections, and waste water/cuttings reinjections. Conversely, near-wellbore fracture tortuosity may be a desirable phenomenon in some particular situations, such as wellbore strengthening treatment in which fracture tortuosity may facilitate the bridging of the fracture and increase sustainable pressure of the wellbore. Therefore,

the capabilities of the proposed numerical model in predicting near-wellbore fracture complexities have significant implications for such field practices.

As mentioned earlier, assuming the rock is an impermeable and linearly elastic material, Mogilevskaia et al. [27] and Jeffrey and Zhang [22] have reported that the near-wellbore fracture tortuosity is controlled by dimensionless parameters β or χ_F , which are functions of the far-field stresses, rock mechanical properties, and injection parameters. However, the simulation results in this paper using a fully coupled poromechanical model have shown that the porous features of the rock can also greatly influence the near-wellbore fracture path and injection pressure. This implies that the fluid flow in the pores, fluid leak-off from the fracture and wellbore surfaces, and their

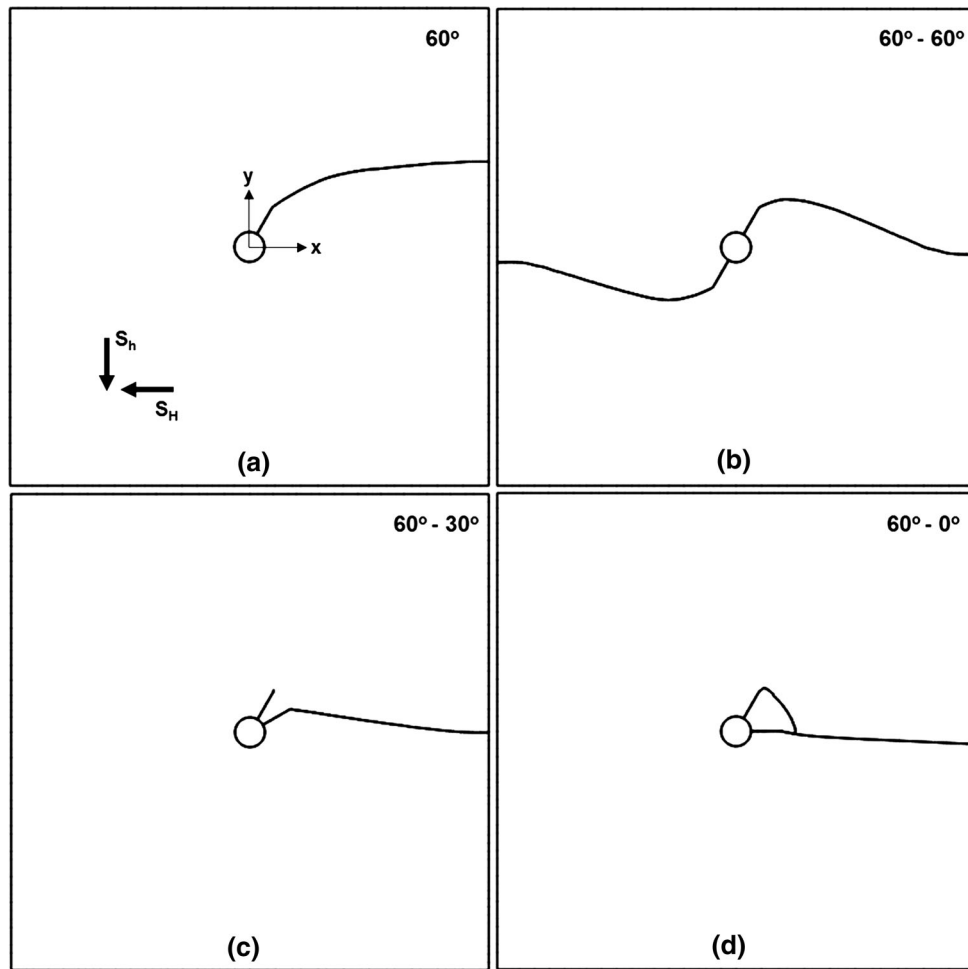


Fig. 23 Fracture trajectories for starter fractures with different orientation angles with respect to the direction of S_H

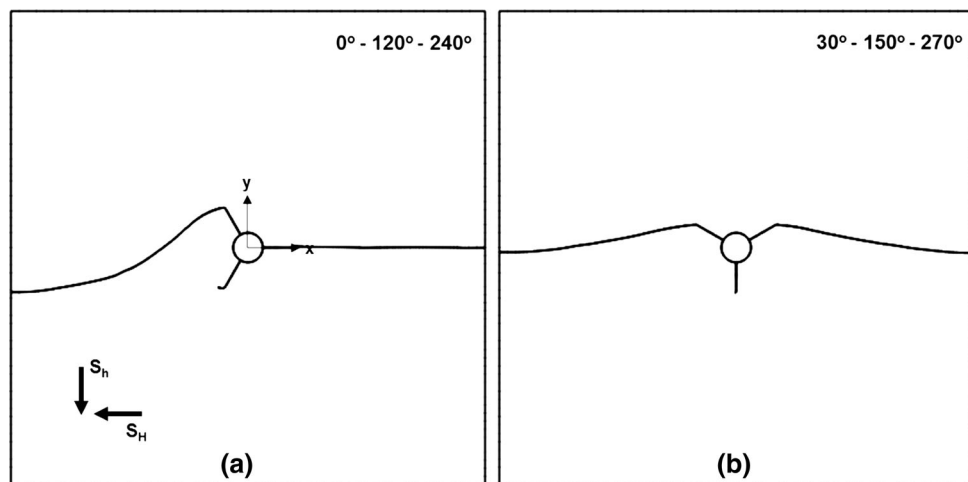


Fig. 24 Fracture trajectories with three competing starter fractures positioned on the wellbore wall

interactions with the solid phase of the formation can significantly affect the stress distribution and thus the fracture behaviors in the near-wellbore region. These important porous effects cannot be considered in the previous models

based on linear elasticity. Unfortunately, for fracture growth from a wellbore in poroelastic rocks, it is extremely difficult, if not impossible, to characterize the fracture path using a single dimensionless parameter as for linear-elastic

rocks because the fracture growth is influenced by so many factors. Therefore, the availability of a fully coupled model as the one proposed in this paper can be very useful for better prediction of near-wellbore fracture complexities with fewer limiting assumptions.

The simulation results of the multiple competing fractures in Sect. 5 indicate that the dominating fracture generally propagates from the starter fracture positioned with a smaller deviation from the preferred propagation direction (i.e., the S_H direction). This result has useful implications for perforation design in fracturing stimulations to generate simpler, less curved fractures. This is especially true when lacking information about field stresses and therefore the preferred fracture direction. In such cases, the use of multiple perforations (starter fractures) can help increase in the chance of creating fractures in the preferred direction [36]. However, the density of the perforations cannot be too high due to near-wellbore stress interference, which may prematurely arrest fracture propagation. For example, Fig. 25 shows the fracture propagations for six perforations with a phasing angle of 60° . Although there are more starter fractures compared with the cases in Fig. 25 and even two of them positioned exactly on the S_H direction, only one fracture fully propagates in this case due to the larger competition between the fractures. It is clear that the cases in Fig. 25 with less perforations have better fracture propagations for improving well productivity. Of course, there are other concerns regarding high density perforations, such as casing stability, which are beyond the scope of this study.

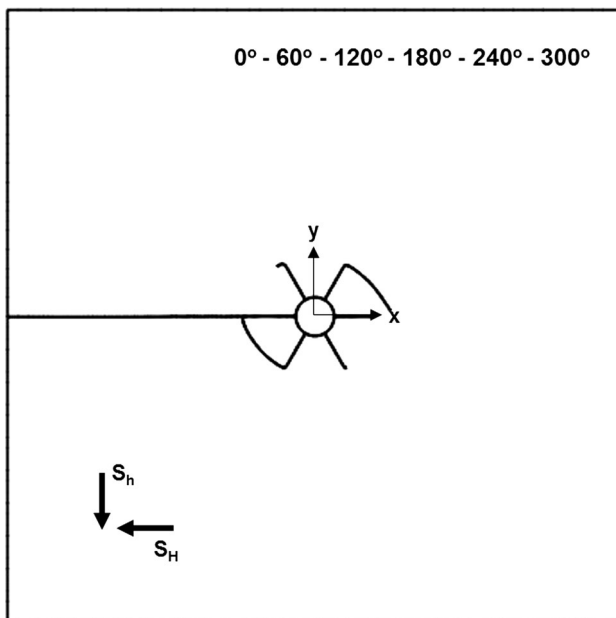


Fig. 25 Fracture trajectories with six competing starter fractures positioned on the wellbore wall

6 Conclusions

In this paper, a fully coupled hydromechanical model is proposed for modeling near-wellbore fracture complexities using the XFEM-based cohesive segment method. The model retains the capability of XFEM on capturing arbitrary fracture paths while considering fluid dynamics in the fracture and poroelastic behaviors of the rock. The model was verified against published experimental results and good agreements were obtained. The model was then used to investigate the factors that influence near-wellbore fracture behaviors. The following conclusions were obtained based on numerical simulation results.

1. The initial loading conditions of the formation, including far-field stresses and pore pressure, can strongly affect near-wellbore fracture behaviors. A larger field stress anisotropy or pore pressure can result in sharper fracture turning in the near-wellbore region. When the stress anisotropy is small enough, the fracture may not be able to reorient itself to the direction of S_H . When the starter fracture has a large deviated angle from the S_H direction, a larger stress anisotropy can lead to a larger breakdown pressure. Given a constant S_h , stress anisotropy and pore pressure do not affect the final fracture propagation pressure.
2. The porous properties of the formation, including permeability and leak-off coefficient that cannot be considered in previous linearly elastic models, also strongly influence near-wellbore fracturing. An increase in permeability or leak-off coefficient generally results in increased severity of fracture curving and decreased injection pressure profile.
3. The elastic properties of the formation, including Young's modulus and Poisson's ratio, influence near-wellbore fracturing as well. Young's modulus does not influence fracture turning trajectory, but a larger Young's modulus causes faster fracture growth, higher injection pressure, and narrower fracture width. To the contrary, Poisson's ratio influences fracture turning trajectory but does not affect the injection pressure and fracture width after the fracture escapes the near-wellbore region. A larger Poisson's ratio tends to increase the severity of fracture curving.
4. The influences of fracture mechanics properties of the formation, including cohesive strength and fracture toughness, are also investigated. The results show that a smaller cohesive strength may lead to a more curving fracture and a lower injection pressure profile. However, the fracture toughness within the range for most sedimentary rocks may have very small influence on near-wellbore fracture behaviors.

5. When multiple competing starter fractures are positioned on the wellbore wall, the dominating fracture generally propagates from the one positioned with a smaller deviation angle from the preferred propagation direction (i.e., the S_H direction). The results manifest the existence of stress interference and non-uniform partition of injection fluid among the fractures. Multiple perforations can help increase the chance of creating fractures in the preferred direction in the absence of field stress information. However, the perforation density should not be too high in order to avoid too much stress interference and premature fracture arrest.

The fully coupled model proposed herein overcomes some limitations of the existing near-wellbore fracturing models based on linear-elastic assumption and predicts more realistic fracture tortuosity and injection pressures. The model provides an attractive tool for design and evaluation of many field operations, for which near-wellbore fracture behaviors play an important role, such as hydraulic fracturing, field injectivity testing, waste water and cuttings reinjection, and wellbore strengthening.

Acknowledgements The authors wish to thank the Wider Windows Industrial Affiliate Program, the University of Texas at Austin, for financial and logistical support of this work. Program support from BHP Billiton, British Petroleum, Chevron, ConocoPhillips, Halliburton, Marathon, National Oilwell Varco, Occidental Oil and Gas, and Shell is gratefully acknowledged. Thanks are due also to Dr. Evgeny Podnos for his manuscript review and suggestions.

References

- Abass HH, Brumley JL, Venditto JJ (1994) Oriented perforations—a rock mechanics view. In: Presented at the SPE annual technical conference and exhibition
- Abdollahipour A, Fatehi Marji M, Yarahmadi Bafghi A, Gholamnejad J (2015) Simulating the propagation of hydraulic fractures from a circular wellbore using the Displacement Discontinuity Method. *Int J Rock Mech Min Sci* 80:281–291
- Al-Busaidi A, Hazzard JF, Young RP (2005) Distinct element modeling of hydraulically fractured Lac du Bonnet granite. *J Geophys Res Solid Earth* 110(B6):B06302
- Areias P, Rabczuk T (2017) Steiner-point free edge cutting of tetrahedral meshes with applications in fracture. *Finite Elem Anal Des* 132:27–41
- Areias P, Rabczuk T, Dias-da-Costa D (2013) Element-wise fracture algorithm based on rotation of edges. *Eng Fract Mech* 110:113–137
- Areias P, Rabczuk T, Camanho PP (2014) Finite strain fracture of 2D problems with injected anisotropic softening elements. *Theor Appl Fract Mech* 72:50–63
- Areias P, Msekh MA, Rabczuk T (2016) Damage and fracture algorithm using the screened Poisson equation and local remeshing. *Eng Fract Mech* 158:116–143
- Behrmann LA, Nolte KG (1999) Perforating requirements for fracture stimulations. *SPE Drill Complet* 14(04):228–234
- Bruno MS, Dorfmann A, Lao K, Honeger C (2001) Coupled particle and fluid flow modeling of fracture and slurry injection in weakly consolidated granular media. In: Presented at the DC Rocks 2001, the 38th U.S. symposium on rock mechanics (USRMS)
- Camanho PP, Dávila CG (2002) Mixed-mode decohesion finite elements for the simulation of delamination in composite materials. NASA/TM-2002-211737, pp 1–37
- Chen M, Jiang H, Zhang GQ, Jin Y (2010) The experimental investigation of fracture propagation behavior and fracture geometry in hydraulic fracturing through oriented perforations. *Pet Sci Technol* 28(13):1297–1306
- Cherny S et al (2009) Two-dimensional modeling of the near-wellbore fracture tortuosity effect. *Int J Rock Mech Min Sci* 46(6):992–1000
- Detournay E (2004) Propagation regimes of fluid-driven fractures in impermeable rocks. *Int J Geomech* 4(1):35–45
- Fallahzadeh SH, Rasouli V, Sarmadivaleh M (2015) An investigation of hydraulic fracturing initiation and near-wellbore propagation from perforated boreholes in tight formations. *Rock Mech Rock Eng* 48(2):573–584
- Feng Y, Gray KE (2016) A fracture-mechanics-based model for wellbore strengthening applications. *J Nat Gas Sci Eng* 29:392–400
- Feng Y, Gray KE (2017) Modeling near-wellbore hydraulic fracture complexity using coupled pore pressure extended finite element method. In: Presented at the 51st U.S. rock mechanics/geomechanics symposium
- Feng Y, Gray KE (2017) Modeling lost circulation through drilling-induced fractures. *SPE J*
- Feng Y, Arlanoglu C, Podnos E, Becker E, Gray KE (2015) Finite-element studies of hoop-stress enhancement for wellbore strengthening. *SPE Drill Complet* 30(01):38–51
- Garagash DI (2006) Propagation of a plane-strain hydraulic fracture with a fluid lag: early-time solution. *Int J Solids Struct* 43(18):5811–5835
- Gordeliy E, Abbas S, Prioul R (2016) Modeling of near-wellbore fracture reorientation using a fluid-coupled 2D XFEM algorithm. In: Presented at the 50th U.S. rock mechanics/geomechanics symposium
- Haddad M, Sepehrnoori K (2015) Simulation of hydraulic fracturing in quasi-brittle shale formations using characterized cohesive layer: stimulation controlling factors. *J Unconv Oil Gas Resour* 9:65–83
- Jeffrey RG, Zhang X (2010) Mechanics of hydraulic fracture growth from a borehole. In: Presented at the Canadian unconventional resources and international petroleum conference
- Li Y, Deng JG, Liu W, Feng Y (2017) Modeling hydraulic fracture propagation using cohesive zone model equipped with frictional contact capability. *Comput Geotech* 91:58–70
- Liu F, Gordon PA, Valiveti DM (2017) Modeling competing hydraulic fracture propagation with the extended finite element method. *Acta Geotech*. <https://doi.org/10.1007/s11440-017-0569-6>
- McClure MW, Horne RN (2014) An investigation of stimulation mechanisms in Enhanced Geothermal Systems. *Int J Rock Mech Min Sci* 72:242–260
- Moës N, Dolbow J, Belytschko T (1999) A finite element method for crack growth without remeshing. *Int J Numer. Methods Eng* 46(1):131–150
- Mogilevskaya SG, Rothenburg L, Dusseault MB (2000) Growth of pressure-induced fractures in the vicinity of a wellbore. *Int J Fract* 104(4):23–30
- Nguyen VP, Lian H, Rabczuk T, Bordas S (2017) Modelling hydraulic fractures in porous media using flow cohesive interface elements. *Eng Geol* 225:68–82

29. Rabczuk T, Belytschko T (2004) Cracking particles: a simplified meshfree method for arbitrary evolving cracks. *Int J Numer Methods Eng* 61(13):2316–2343
30. Rabczuk T, Belytschko T (2007) A three-dimensional large deformation meshfree method for arbitrary evolving cracks. *Comput Methods Appl Mech Eng* 196(29):2777–2799
31. Rabczuk T, Song J-H, Belytschko T (2009) Simulations of instability in dynamic fracture by the cracking particles method. *Eng Fract Mech* 76(6):730–741
32. Rabczuk T, Zi G, Bordas S, Nguyen-Xuan H (2010) A simple and robust three-dimensional cracking-particle method without enrichment. *Comput Methods Appl Mech Eng* 199(37):2437–2455
33. Remmers JJC, de Borst R, Needleman A (2008) The simulation of dynamic crack propagation using the cohesive segments method. *J Mech Phys Solids* 56(1):70–92
34. Ren H, Zhuang X, Cai Y, Rabczuk T (2016) Dual-horizon peridynamics. *Int J Numer Methods Eng* 108(12):1451–1476
35. Renc H, Zhuang X, Rabczuk T (2017) Dual-horizon peridynamics: a stable solution to varying horizons. *Comput Methods Appl Mech Eng* 318:762–782
36. Sepehri J, Soliman MY, Morse SM (2015) Application of extended finite element method to simulate hydraulic fracture propagation from oriented perforations. In: Presented at the SPE hydraulic fracturing technology conference
37. Silling SA (2000) Reformulation of elasticity theory for discontinuities and long-range forces. *J Mech Phys Solids* 48(1):175–209
38. Simulia DS (2016) Abaqus analysis user's manual. Dassault Systemes, Providence
39. Snow DT (1969) Anisotropic permeability of fractured media. *Water Resour Res* 5(6):1273–1289
40. Song J-H, Areias PMA, Belytschko T (2006) A method for dynamic crack and shear band propagation with phantom nodes. *Int J Numer Methods Eng* 67(6):868–893
41. Terzaghi K (1943) Theory of consolidation. In: *Theoretical soil mechanics*. Wiley, New York 1943, pp 265–296
42. Turon A, Camanho PP, Costa J, Dávila CG (2006) A damage model for the simulation of delamination in advanced composites under variable-mode loading. *Mech Mater* 38(11):1072–1089
43. Vermeer PA, Verruijt A (1981) An accuracy condition for consolidation by finite elements. *Int J Numer Anal Methods Geomech* 5(1):1–14
44. Wang T, Liu Z, Zeng Q, Gao Y, Zhuang Z (2017) XFEM modeling of hydraulic fracture in porous rocks with natural fractures. *Sci China Phys Mech Astron* 60(8):084612
45. Weng X (1993) Fracture initiation and propagation from deviated wellbores. In: Presented at the SPE annual technical conference and exhibition
46. Wu K, Olson JE (2016) Mechanisms of simultaneous hydraulic-fracture propagation from multiple perforation clusters in horizontal wells. *SPE J* 21(03):1000–1008
47. Wu K, Olson J, Balhoff MT, Yu W (2017) Numerical analysis for promoting uniform development of simultaneous multiple-fracture propagation in horizontal wells. *SPE Prod Oper* 32(01):41–50
48. Yao Y (2012) Linear elastic and cohesive fracture analysis to model hydraulic fracture in brittle and ductile rocks. *Rock Mech Rock Eng* 45(3):375–387
49. Zhang X, Jeffrey RG, Thiercelin M (2007) Deflection and propagation of fluid-driven fractures at frictional bedding interfaces: a numerical investigation. *J Struct Geol* 29(3):396–410
50. Zhang GM, Liu H, Zhang J, Wu HA, Wang XX (2010) Three-dimensional finite element simulation and parametric study for horizontal well hydraulic fracture. *J Pet Sci Eng* 72(3–4):310–317
51. Zhang X, Jeffrey RG, Bungler AP, Thiercelin M (2011) Initiation and growth of a hydraulic fracture from a circular wellbore. *Int J Rock Mech Min Sci* 48(6):984–995
52. Zhang X, Jeffrey RG, Bungler AP (2011) Hydraulic fracture growth from a non-circular wellbore. In: Presented at the 45th U.S. rock mechanics/geomechanics symposium
53. Zhao P, Santana CL, Feng Y, Gray KE (2017) Mitigating lost circulation: a numerical assessment of wellbore strengthening. *J Pet Sci Eng* 157:657–670
54. Zhou X, Burbey TJ (2014) Fluid effect on hydraulic fracture propagation behavior: a comparison between water and supercritical CO₂-like fluid. *Geofluids* 14(2):174–188
55. Zhou J, Zhang L, Pan Z, Han Z (2016) Numerical investigation of fluid-driven near-borehole fracture propagation in laminated reservoir rock using PFC2D. *J Nat Gas Sci Eng* 36:719–733
56. Zhou J, Zhang L, Braun A, Han Z (2017) Investigation of processes of interaction between hydraulic and natural fractures by PFC modeling comparing against laboratory experiments and analytical models. *Energies* 10(7):1001
57. Zhu H, Guo J, Zhao X, Lu Q, Luo B, Feng Y-C (2014) Hydraulic fracture initiation pressure of anisotropic shale gas reservoirs. *Geomech Eng* 7(4):403–430